Cell Reports
Medicine

Article

Detecting altered hepatic lipid oxidation by MRI in an animal model of MASLD

Graphical abstract

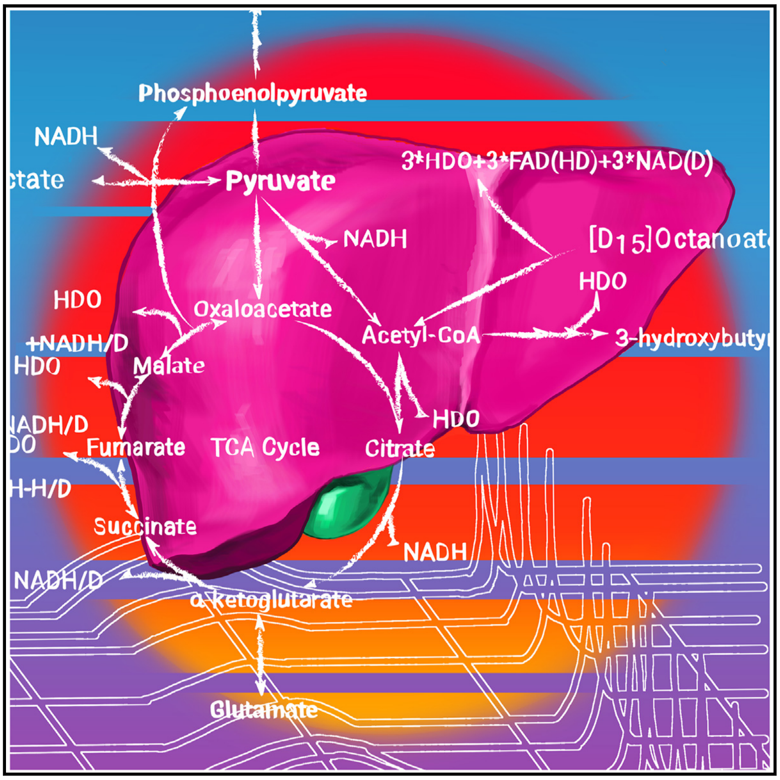

Authors

Marc McLeod, Mario C. Chang,
Anna Rushin, ..., James A. Bankson,
Kenneth Cusi, Matthew E. Merritt

Correspondence

matthewmerritt@ufl.edu

In brief

McLeod et al. demonstrate that fatty acid β-oxidation can be detected by deuterium MRI using [D_{15}]octanoate as the contrast agent. A high-fat diet mouse model of MASLD demonstrates elevated whole-liver oxidation, while relative oxidative efficiency declines with weeks on diet.

Highlights

- The mouse liver oxidizes [D_{15}]octanoate, producing partially deuterated water (HDO)
- In perfused mouse liver, a dietary model of MASLD leads to increased β-oxidation
- MRI after injection of [D_{15}]octanoate tracks with MASLD progression
- HDO is retained in the mitochondrial matrix after octanoate oxidation

McLeod et al., 2024, Cell Reports Medicine *5*, 101714
September 17, 2024
https://doi.org/10.1016/j.xcrm.2024.101714

CellPress

Cell Reports Medicine

Article

Detecting altered hepatic lipid oxidation by MRI in an animal model of MASLD

Marc McLeod,[1,2] Mario C. Chang,[1] Anna Rushin,[1] Mukundan Ragavan,[1,3] Rohit Mahar,[4] Gaurav Sharma,[1] Arshee Badar,[1] Anthony Giacalone,[1] Max E. Glanz,[1] Vinay R. Malut,[1] Dalton Graham,[1] Nishanth E. Sunny,[5] James A. Bankson,[6] Kenneth Cusi,[7] and Matthew E. Merritt[1,8,*]

[1]Department of Biochemistry and Molecular Biology, University of Florida College of Medicine, Gainesville, FL 32610, USA
[2]University of Texas Southwestern Medical Center, 5323 Harry Hines Boulevard, Dallas, TX 75390-9014, USA
[3]Department of Structural Biology, St. Jude Children's Research Hospital, Memphis, TN 38105, USA
[4]Department of Chemistry, Hemvati Nandan Bahuguna Garhwal University (A Central University), Srinagar Garhwal, Uttarakhand 246174, India
[5]Department of Animal and Avian Sciences, University of Maryland, College Park, MD 20742, USA
[6]Department of Imaging Physics, The University of Texas MD Anderson Cancer Center, 1515 Holcombe Boulevard, Houston, TX 77030-4009, USA
[7]Division of Endocrinology, Diabetes, and Metabolism, Department of Medicine, Veterans Health Administration and University of Florida, Gainesville, FL 32610, USA
[8]Lead contact
*Correspondence: matthewmerritt@ufl.edu

https://doi.org/10.1016/j.xcrm.2024.101714

SUMMARY

Metabolic dysfunction-associated steatotic liver disease (MASLD) prevalence is increasing annually and affects over a third of US adults. MASLD can progress to metabolic dysfunction-associated steatohepatitis (MASH), characterized by severe hepatocyte injury, inflammation, and eventual advanced fibrosis or cirrhosis. MASH is predicted to become the primary cause of liver transplant by 2030. Although the etiology of MASLD/MASH is incompletely understood, dysregulated fatty acid oxidation is implicated in disease pathogenesis. Here, we develop a method for estimating hepatic β-oxidation from the metabolism of [D_{15}]octanoate to deuterated water and detection with deuterium magnetic resonance methods. Perfused livers from a mouse model of MASLD reveal dysregulated hepatic β-oxidation, findings that corroborate *in vivo* imaging. The high-fat-diet-induced MASLD mouse studies indicate that decreased β-oxidative efficiency in the fatty liver could serve as an indicator of MASLD progression. Furthermore, our method provides a clinically translatable imaging approach for determining hepatic β-oxidation efficiency.

INTRODUCTION

The incidence of metabolic dysfunction-associated steatotic liver disease (MASLD), previously referred to as non-alcoholic fatty liver disease (NAFLD), has risen rapidly over the last few decades and affects more than 30% of adults in the US.[1–3] MASLD is defined as ≥5% of hepatocytes having macrovesicular steatosis in the absence of a secondary cause of steatosis and with at least one of the following cardiometabolic phenotypes: having overweight or obesity, prediabetes or type 2 diabetes, hypertension, and/or atherogenic dyslipidemia.[4] Of individuals with MASLD and obesity and/or type 2 diabetes, ∼15%–20% are expected to progress to the more severe form with metabolic dysfunction-associated steatohepatitis (MASH),[5–7] previously referred to as non-alcoholic steatohepatitis (NASH), characterized by steatosis with inflammation and hepatocyte injury (also known as hepatocyte ballooning), with or without evidence of liver fibrosis.[1,2] Although MASLD can lead to MASH in some cases, the factors triggering this transition are not well established.[1,2,6,8] Unfortunately, many individuals with MASH develop liver cirrhosis, and MASH now stands as the number two cause of liver transplants in the US.[7] As viral hepatitis and chronic viral liver disease continue to decline, MASH is predicted to be the number one cause of transplantation by 2030.[4] A high percentage of adults with obesity, especially with type 2 diabetes,[5,6,8] have steatosis (>70%), and about half develop MASH.[5,9]

Current guidelines follow an algorithm for the diagnosis of MASLD centered around obesity, presence of type 2 diabetes, and cardiometabolic risk. Such individuals are risk stratified based on a combination of non-invasive tests (NITs) from diagnostic panels (such as FIB-4 that integrates into an equation age, AST, ALT, and platelet count) to proprietary MASLD biomarkers (e.g., Enhanced Liver Fibrosis [ELF], others) and imaging (e.g., vibration-controlled transient elastography [VCTE] or magnetic resonance imaging [MRI] of hepatic fat or fibrosis).[1,2,10] Additionally, liver biopsy is recommended for patients with MASLD to definitively diagnose MASH and stage the disease.[1,2] However, the diagnostic accuracy of liver biopsy is limited by sampling error, and such biopsies have a known risk of morbidity.[1] Despite this clear protocol for identifying MASLD

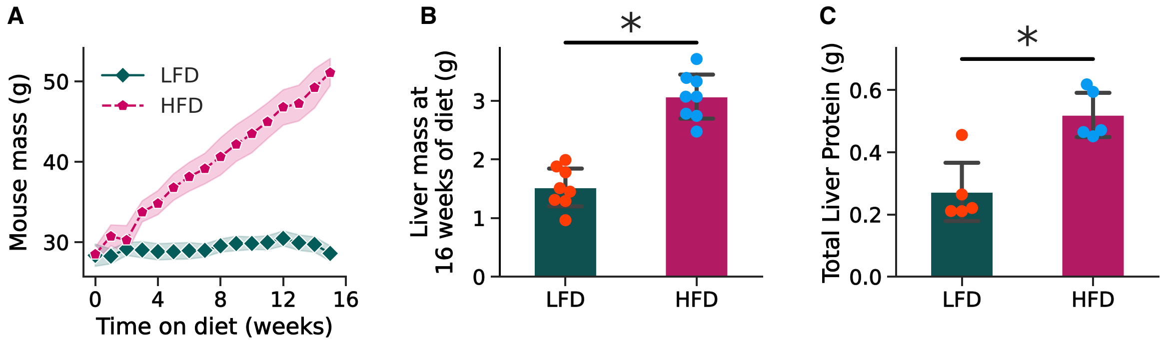

Figure 1. Changes in mouse body weight, liver weight, and total liver protein over 16 weeks of HFD or LFD

(A) Weekly mouse mass of 10-week-old C57BL/6J mice after switching to a high-fat diet (HFD; 60% fat by Kcal) or a low-fat diet (LFD; 10% fat by Kcal; $n = 10$ for each group). Data are presented as average ± 95% confidence interval (CI; shaded regions).

(B and C) Livers of mice on the indicated diets for 16 weeks were collected after *ex vivo* perfusion. Total liver mass was measured ($n = 8$ for LFD and HFD) (B) and total liver protein was quantified by Bradford assay ($n = 5$ for LFD and HFD) (C).

Error bars represent the mean ± standard deviation. Statistical significance was determined by analysis of covariance for mouse weight gain and Student's t test for liver mass and total liver protein ($^{*}p < 0.05$).

and MASH, the diagnosis remains a challenge both for research clinical trials and in the clinic.[6] Current clinical guidelines recommend weight loss by means of lifestyle intervention[1,2,10] plus use of pharmacotherapy for the management of obesity or type 2 diabetes with agents known to reverse steatohepatitis, such as pioglitazone or glucagon-like peptide-1 receptor agonists (GLP-1RAs).[11] Resmetirom, a thyroid hormone receptor beta (THR-β) agonist that reverses steatohepatitis by improving hepatic conversion of T4 to T3 and enhancing mitochondrial function, was recently approved as the first drug to treat MASH by the US Food and Drug Administration.[12,13]

Because obesity is so commonly associated with hepatic steatohepatitis, understanding how the accumulation of excess hepatic lipids is associated with insulin resistance and activation of inflammatory pathways is essential to develop better targeted treatments in MASLD.[5,6,8] However, these mechanisms are still poorly understood. Lipid accumulation, especially of free fatty acids, leads to endoplasmic reticulum (ER) stress and subsequent lipoapoptosis resulting from increased ceramide production.[14,15] In some models of MASLD, decreased oxidative metabolism has been used to infer reduced fatty acid β-oxidation as a culprit for the accumulation of toxic levels of lipids.[16] However, in several obesity models of MASLD, higher hepatic lipids correlate with increased oxidative metabolism,[17–19] potentially to relieve ER stress and lipoapoptosis. However, this increase in oxidative metabolism drives reactive oxygen species (ROS) production that can induce mitochondrial DNA (mtDNA) damage and trigger inflammatory pathways.[20] Furthermore, increased β-oxidation is associated with greater levels of ROS production than those produced by tricarboxylic acid (TCA) cycle activity and appears a likely culprit for driving ROS-induced damage during MASLD progression in the setting of adipose tissue insulin resistance and increased lipolysis and flux of fatty acids to the liver.[5,6,20] However, current methods infer β-oxidative flux using fatty acid oxidation products such as ketones or by differences between the estimated TCA cycle turnover and oxidation of substrates other than fatty acids. Direct assessment of hepatic β-oxidation would enhance our understanding of the disease process.

Deuterated fatty acids produce deuterated water (HDO) as a direct byproduct of β-oxidation,[21] enabling specific, localized spectroscopy or MRI of hepatic β-oxidation. Previously, we used simple MRI protocols to monitor HDO production resulting from glucose metabolism in the rodent brain following bolus administration of $[^{2}H_{7}]$glucose.[22] Here, we used $[^{2}H_{15}]$octanoate (also referred to as $[D_{15}]$octanoate) as a metabolic contrast agent to study hepatic fatty acid metabolism in a mouse model of high-fat diet (HFD)-induced MASLD.[23] We selected octanoate because it does not require albumin for administration and readily diffuses into the liver mitochondria, unlike long-chain fatty acids, which are poorly soluble and must be complexed with albumin for delivery and require carnitine palmitoyl transferase-1 (CPT-1) to enter the mitochondria.[24,25] Additionally, the rapid uptake of octanoate suppresses the activity of the TCA cycle,[26] enabling selective detection of HDO produced from β-oxidation by deuterium magnetic resonance (DMR). Our method operates in analogy to the glucose tolerance test in which the excess substrate enforces changes in metabolism. We hypothesize that this deuterated "lipid challenge" test will be diagnostic of disease state.

RESULTS

Deuterium metabolic spectroscopy of $[D_{15}]$octanoate-perfused liver reveals reduced hepatic β-oxidation per gram of liver protein in a mouse model of MASLD

As a model, we used control mice on a low-fat diet (LFD; composed of 10% fat by calories) and mice on an HFD (60% fat by calories). The mice on the HFD almost doubled in body weight at the 16 week time point (51 ± 2.3 g SD) relative to mice on the LFD (28.6 ± 1.2 g SD) (Student's t test, $p = 1.2E{-}6$) (Figure 1A). Additionally, perfused livers from fasted, HFD mice were significantly larger (3.1 ± 0.25 g, $p = 4.5E{-}5$) than their fasted, LFD counterparts (1.6 ± 0.32 g) and had significantly more total liver protein (Figures 1B and 1C), conditions also observed for patients with MASLD.[6]

To assess the rate of β-oxidation in the *ex-vivo*-perfused liver, we measured HDO elution as a byproduct of $[D_{15}]$octanoate oxidation (Figures 2A and S1). Because HDO is present at natural abundance (~0.031%) in body water,[27] we first assessed HDO by nuclear magnetic resonance (NMR) analysis prior to the perfusion of $[D_{15}]$octanoate (Figure 2B, red trace). We then monitored the increase in HDO after $[D_{15}]$octanoate perfusion (Figure 2B, blue trace), which we set as the start of the period for monitoring HDO. We initially detected an exponential increase in HDO, followed by a slower, stable increase in HDO that was similar for livers from HFD or LFD mice (Figure 2C). After normalizing for endogenous (pre-perfusion) HDO, we observed that $[D_{15}]$octanoate accumulated to a greater extent in the livers of the HFD mice than the livers of the LFD mice (Figure 2D). Normalizing HDO produced by total liver protein showed that the livers of the HFD mice produced less HDO than those of the LFD mice (Figure 2E). Finally, we normalized the HDO signal to the $[D_{15}]$octanoate signal to assess the balance between fatty acid oxidation and storage during perfusion. Livers that oxidize more fatty acid than they store will have a higher ratio. Livers of LFD mice had higher ratios than livers of HFD mice (Figure 2F). Collectively, these data indicated that livers of HFD mice have reduced efficiency in β-oxidation compared to livers of LFD mice.

Analysis of perfusate confirms perturbed β-oxidation in a mouse model of MASLD

To assess the reliability of our NMR-based β-oxidation analysis, we measured hepatic consumption of $[D_{15}]$octanoate from the efferent perfusate over the course of perfusion by gas chromatography-mass spectrometry (GC-MS). Although total $[D_{15}]$octanoate consumption was similar in the livers from the two groups (Figure 2G), $[D_{15}]$octanoate consumption was significantly lower in the livers from the HFD mice when normalized to total liver protein: HFD mouse livers consumed 3.84 ± 0.60 μmol/min/g liver protein, and LFD mouse livers consumed 7.04 ± 1.80 μmol/min/g liver protein (Figure 2H). These results confirmed the accuracy of the HDO analysis to monitor fatty acid β-oxidation from $[D_{15}]$octanoate.

The rate of ketogenesis was also measured from the effluent perfusate for comparison to prior methods of inferring β-oxidation rates as well as for metabolic modeling efforts. The HFD group had a ~2-fold higher rate of total ketone production than the LFD group (0.85 ± 0.14 vs. 0.41 ± 0.13 μmol/min) (Figure 2G). However, these rates were not significantly different when normalized for total liver protein (Figure 2H), indicating that hepatomegaly is the primary source of overall increased ketogenesis. Additionally, gluconeogenesis rates were measured to assess the contributions of unlabeled pyruvate and lactate during perfusion. Total gluconeogenesis rates were insignificantly elevated in the HFD group ($p = 0.12$) compared to the LFD group (Figure 2G). No trend was observed in relative gluconeogenesis rates (Figure 2H).

Metabolic modeling of MASLD mouse perfused livers reveals increased β-oxidative activity but a decline in β-oxidative metabolism per gram of liver protein

To assess global oxidative metabolism in the liver (Figure 3A), we calculated oxygen consumption during perfusion as the difference in O_2 from the afferent and efferent perfusate. Despite the increased liver size after HFD, the total oxygen consumption levels of livers from mice on LFD (2.2 μmol O_2/min) and HFD (2.25 μmol O_2/min) were similar (Figure 3B, left). When normalized for liver protein, oxygen consumption was significantly less in livers from mice on an HFD (4.2 μmol O_2/min/g liver protein) than those on an LFD (8.9 μmol O_2/min/g liver protein) (Figure 3B, right). Thus, we inferred that the larger livers of the HFD mice had less active oxidative phosphorylation per gram of liver protein than the livers of the LFD mice.

To determine specific differences in the oxidative pathways of β-oxidation and the TCA cycle, we built a model with isotopomer network compartmental analysis (INCA) (Figures 3A and S1; Table S1).[28] The inputs to the model were as follows: the concentration and isotopologue enrichments of citrate as an indicator of acetyl-CoA incorporated into the TCA cycle; glutamate to capture exchange with α-ketoglutarate; succinate to estimate exchange of 4-carbon TCA cycle intermediates; the rate of ketogenesis, determined by 3-hydroxybutyrate production; oxygen consumption; and the rate of gluconeogenesis. We used GC-MS to measure the pool sizes and isotopologue distributions of metabolites in liver tissue samples and the effluent of livers simultaneously perfused with $[D_{15}]$octanoate and natural abundance pyruvate and lactate. Of the metabolite pools, only liver-derived alanine showed a significant difference between HFD and LFD mice when normalized for liver protein (Figure S2). The fractional enrichment of the deuterium label in 3-hydroxybutyrate, citrate, glutamate, and succinate across all isotopomers was similar in livers from either HFD or LFD mice (Figures 3C and 3S). The estimated acetyl-CoA enrichment of ~35.5%–38% was conserved among livers from both groups and extrapolated from citrate enrichment after adjusting for the loss of one-third of the deuterium label resulting from M+1 acetyl-CoA condensation with oxaloacetate. Ketone-extrapolated acetyl-CoA enrichment agreed with this measure after adjusting for multiple labeling by two acetyl-CoA units. Adjustment was achieved by halving 3-hydroxybutyrate enrichment and correcting for the loss of one-third of the deuterium label resulting from M+1 acetyl-CoA condensation with acetoacetyl-CoA. The resulting flux estimates demonstrate a clear perturbation of oxidative metabolism (Figure 3D). Average 95% confidence intervals for parametric optimization of flux (Table S2) demonstrate that elevated oxidative metabolism is consistently congruent with the data. This trend was preserved for the confidence intervals of flux estimates between perfused livers (Table S3).

Both the TCA cycle and β-oxidation produce nicotinamide adenine dinucleotide (NADH) and flavin adenine dinucleotide ($FADH_2$) (Figures 3A and S1). These two sources of reducing equivalents can be oxidized by the oxidative phosphorylation complex for ATP production. We observed a significantly higher total β-oxidative flux (octanoate oxidation) and $FADH_2$ turnover in livers of the HFD group than those of the LFD group (Figure 3D). When normalized for the differences in liver protein, the livers of the HFD mice had less efficient oxidation of octanoate and significantly reduced $FADH_2$ oxidation with a trend toward lower NADH oxidation (Figure 3E, right). The reduced $FADH_2$ and NADH oxidation in the HFD mouse livers per gram of liver protein provides an explanation for the observed decrease in O_2 consumption per

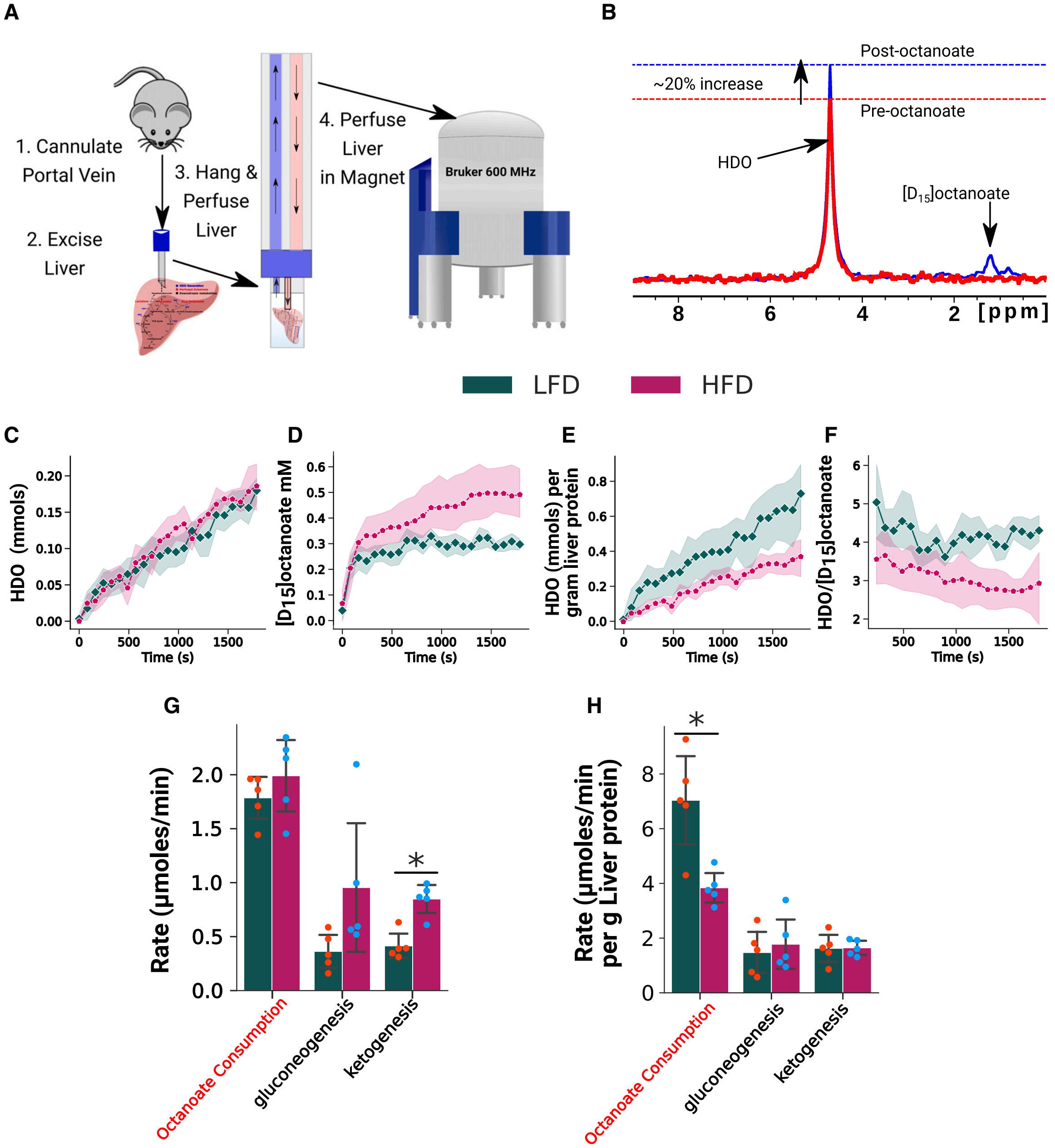

Figure 2. Measures of oxidative metabolism in an *ex-vivo*-perfused liver system

(A) Diagram of in-magnet perfused mouse liver setup.

(B) Representative trace of deuterium magnetic resonance spectroscopy of perfused mouse liver before (red) and 30 min after (blue) perfusion with $[D_{15}]$ octanoate.

(C–F) Quantification of HDO and $[D_{15}]$octanoate peaks presented as average ± 95% CI of individual liver signal in shaded regions ($n = 5$ for each group).

(C) HDO (mmol) produced throughout liver perfusion from $[D_{15}]$octanoate.

(D) mM $[D_{15}]$octanoate in liver during perfusion.

(E) Total HDO per gram of liver protein produced throughout liver perfusion from $[D_{15}]$octanoate.

(F) Ratio of HDO signal intensity to $[D_{15}]$octanoate signal intensity.

(G and H) Total (G) and normalized (H) rates of the indicated metabolic processes were determined by GC-MS and quantified from changes in the concentrations of $[D_{15}]$octanoate, glucose, and ketones ($n = 5$ for each group).

Statistical significance was determined by analysis of covariance for NMR quantification and Student's t test (two-tailed) for GC-MS rate comparisons ($^{*}p < 0.05$).

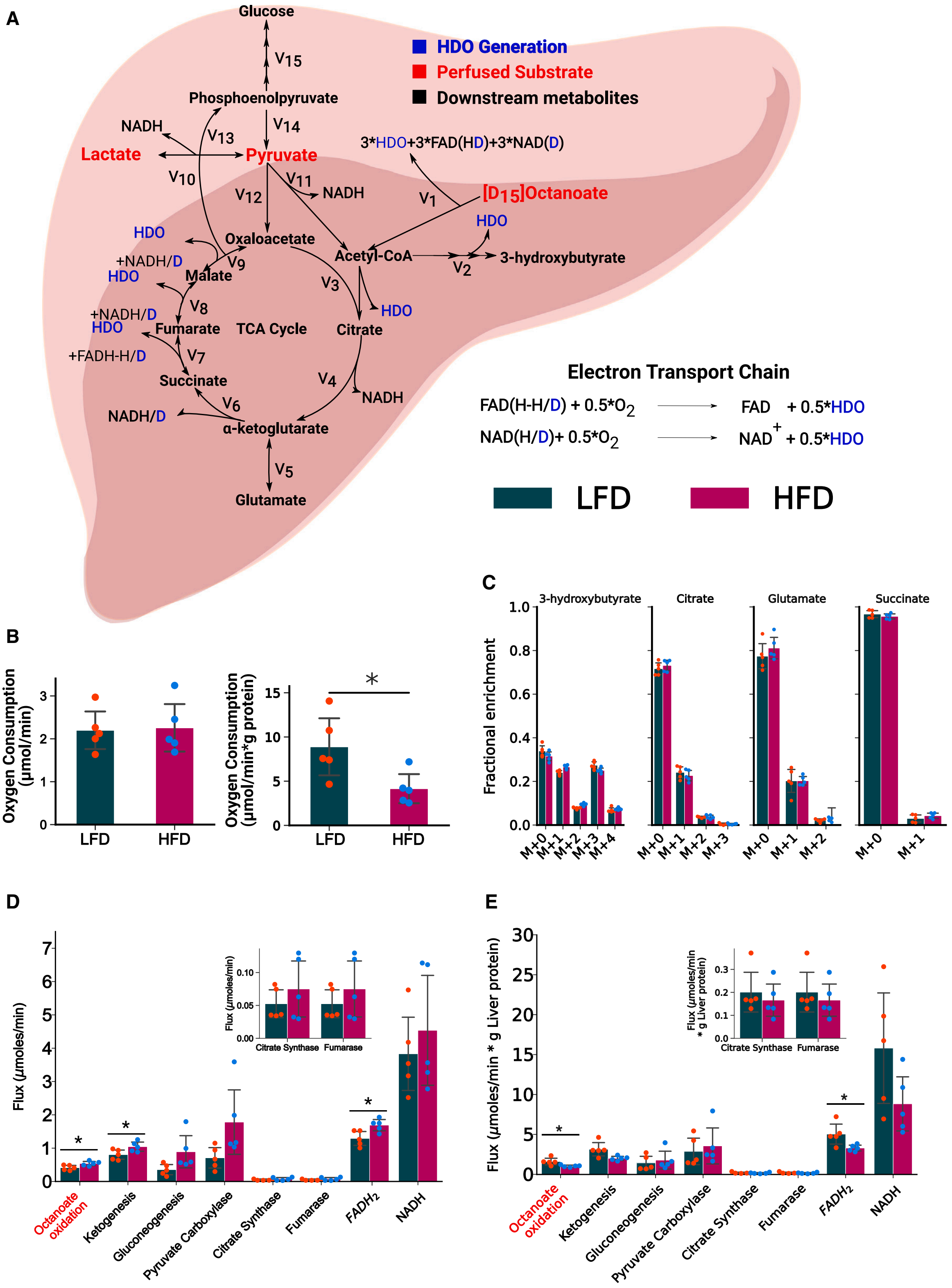

Figure 3. Metabolic modeling of flux in an *ex-vivo*-perfused liver

(A) Diagram of INCA metabolic model used to define the rates of [D_{15}]octanoate consumption, electron transport chain activity, and central carbon metabolism.

(legend continued on next page)

gram of liver protein. Glucagon perfused livers showed the expected increases in octanoate oxidation (Figure S4).

MASLD mouse livers exhibit similar abundance of most proteins or transcripts of proteins involved in oxidative metabolism

To determine if there were differences in the relative amounts of proteins involved in oxidative metabolism in the livers of mice on the two diets, we measured protein abundance of complex 1–5 for the mitochondrial electron transport chain, CPT1, and long-chain acyl-CoA dehydrogenase (LCAD) (Figures S5A and S5B). We observed no significant differences in the amounts of these proteins between livers from HFD and LFD mice (Figures S5A and S5B). Additionally, we measured mRNA transcript abundance by qPCR of *LCAD* and *HMG-CS2*, encoding hydroxymethylglutaryl-CoA synthetase 2 (Figures S5C and S5D). *HMG-CS2* mRNA was significantly lower in livers from the HFD animals than those from LFD animals (Figure S5C). These data indicated that the source of dysfunction driving the differences in β-oxidation was not aberrant protein expression of fatty acid transporters or dehydrogenases.

DMRI detects hepatic fatty acid oxidation *in vivo*

To assess whether [D_{15}]octanoate can serve as a contrast reagent for assessing liver-specific metabolism, we performed deuterium MRI (DMRI) with 12-week-old C57BL/6J mice administered [D_{15}] octanoate by tail vein injection (Figure S6). By 24 min after [D_{15}]octanoate administration, the deuterated signal localized to the liver and was visible by ^{2}H fast low-angle single shot (FLASH) imaging (Figures 4A–4C, yellow circle). Two-point Dixon (2PD) imaging, 52 min post-injection, indicated that most of the deuterated signal was from HDO (Figure 4B).

To confirm that the localized signal was primarily from an increase in the HDO signal, we also performed a spectroscopic analysis of the torso of fed mice administered [D_{15}]octanoate while in the 11 T MRI magnet (Figures 4D and 4E). We observed time-dependent changes in the [D_{15}]octanoate and HDO signal intensities, with octanoate originally rising and then tailing off, while the HDO signal increased more quickly in the beginning and then adopted a slower rate of appearance (Figure 4E). The [D_{15}]octanoate signal peaked at ∼5 min post-injection and remained stable for 25–30 min after injection before slowly declining until 60 min post-injection. The HDO signal rapidly increased from 0 to 30 min, followed by a slower rate of increase before peaking at ∼60 min after injection (Figure 4E).

DMRI detects dysregulated β-oxidation in MASLD mice

Having established that we successfully monitored fatty acid β-oxidation by DMRI using [D_{15}]octanoate as the contrast label, we tested if we could detect changes in the rate of β-oxidation between *ad libitum* chow-fed and fasted mice in a progressive MASLD mouse model. We transitioned to a chow diet control for the *in vivo* experiments to more accurately model current human nutritional profiles that result in consistent weight gain. We performed DMRI of C57BL/6J mice on HFD for 0, 8.5, 17, 24, and 36 weeks and compared them to mice on the normal chow diet (Figures 5A and 5B). We monitored body weight and calorie consumption for both groups of mice, which showed that the HFD mice consumed more calories and had greater overall mass compared to the mice with *ad libitum* access to a normal chow diet (Figure S7A). The rate of weight gain by the mice with *ad libitum* access to normal chow was stable throughout the experiment, whereas the mice with *ad libitum* access to the HFD showed a faster rate of increase for the first 8 weeks and then a rate similar to that of the mice on the normal chow diet. Based on a histological assessment of steatosis, elevated liver triglyceride levels, abdominal obesity, and elevated fasting blood glucose, the HFD animals had MASLD from 8 weeks of diet onward (Figures 5C, S7, and S8; Tables S4, S5, S6, and S7). Overnight-fasted animals on HFD and chow diet had similar liver triglyceride content, potentially a side effect of increased lipolysis and sourcing of extrahepatic fat to the liver for processing and ketogenesis (Figure S8, left). However, we estimated that greater than 5% of hepatic weight was comprised of triglycerides in HFD *ad libitum*-fed animals from 8.5 weeks onward (Figure S8 right; Table S5).

Consistent with the increase in liver mass that we observed for mice on 16 weeks of HFD (Figure 1B), the imaged livers appeared larger in the mice on the HFD compared with those on normal chow (Figures 5A and 5B). We detected an HDO signal following [D_{15}]octanoate injection in both fed and fasted control mice on a normal chow diet as well as mice on the HFD (Figures 5A and 5B). We noted that the HDO signal became more punctate and less uniformly distributed in both the HFD- and normal-chow-fed mice (Figure 5B), suggesting that metabolism changed as the mice aged during the course of the experiment. This highly intense, punctate HDO signal was notable in both the fed and fasted states at 24 weeks of HFD. Note that the data were not apodized, and no mask based on the ^{1}H image was used to suppress out-of-volume artifacts. Apodization with a Fermi function removes the punctate nature of the images. We present these data in their rawest form to emphasize the general quality of the imaging paradigm.

To account for changes in liver size during disease progression, we quantified liver mass for mice in the fasted or fed state at baseline and 8.5, 17, 24, and 36 weeks on each diet (Figure 6A; Table S6). Comparing liver mass in the fed state confirmed that chow diet mice had significantly increased liver mass at 17, 24,

---

(B) Oxygen consumption was monitored by Hansatech oxygraph+ of afferent and efferent perfusate in [D_{15}]octanoate-perfused livers from mice in LFD and HFD groups. Rates of total oxygen consumption and O_2 consumption normalized to gram of liver protein are shown.

(C) Fractional enrichments of 3-hydroxybutyrate to represent ketones, citrate as an indicator of TCA cycle enrichment and acetyl-CoA partitioned into the TCA cycle, glutamate as an exchangeable portion of the TCA cycle with α-ketoglutarate, and succinate to represent the second half of the TCA cycle exchanging with fumarate.

(D and E) Predicted flux for the mouse perfused liver by INCA metabolic modeling of (D) total flux per liver and (E) relative flux per gram of liver protein.

Error bars represent mean ± standard deviation (*n* = 5 for each group). Statistical significance was determined by Student's t test (two-tailed) for rate comparisons (*$p < 0.05$).

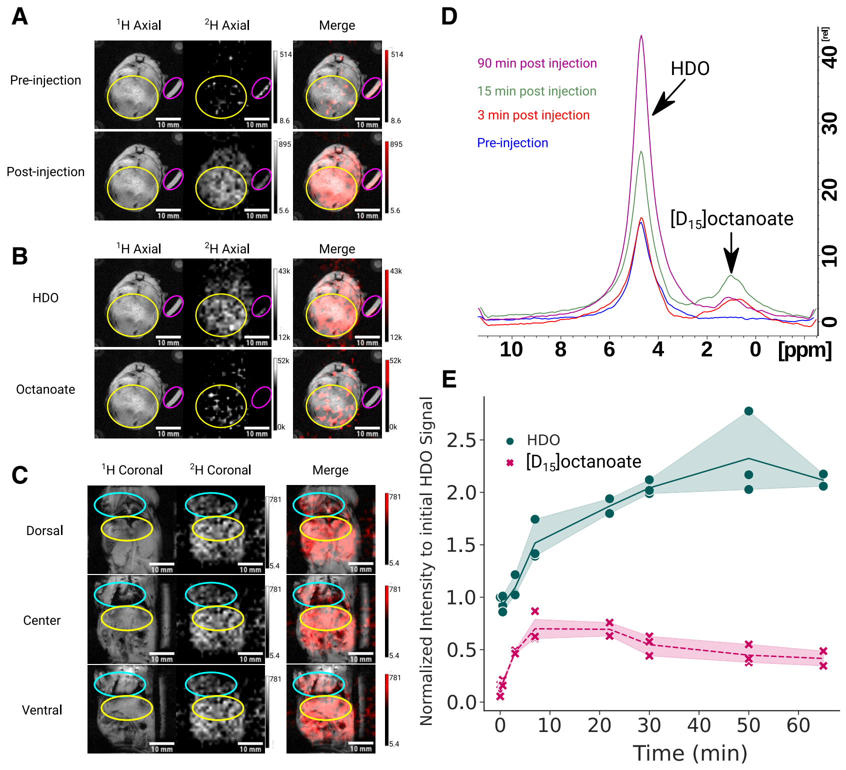

Figure 4. Metabolic characterization of *ad-libitum*-fed 12-week-old C57BL/6J mouse torso through magnetic resonance imaging and spectroscopy

(A–C) Images are represented using a ^{1}H volume coil (column 1) and a ^{2}H saddle coil (column 2) with ^{1}H (grayscale) and ^{2}H (red) merges of the two (column 3). The liver is circled in yellow, and the 0.05% D_2O standard is circled in magenta. Axial FLASH images through the mouse vertical cross-section are taken with respect to the liver in ^{1}H and ^{2}H modes. The images in (A) represent the signal prior to (pre-injection) and 24 min post- (post-injection) [D_{15}]octanoate administration. Overlays of the ^{1}H and ^{2}H axial images demonstrate localization of the signal to the liver after administration of [D_{15}]octanoate tracer. Representative 2PD images obtained 52 min after [D_{15}]octanoate injection are shown in (B). In (C), for the coronal images taken 80 min post-injection, the heart and shoulder are circled in teal, and the liver is circled in yellow.

(D and E) Spectral analysis of fed mouse torso post-tail vein injection of [D_{15}]octanoate. Data shown represent a single representative fed mouse. In (D), the spectral overlay of whole-volume, deuterium, single-pulse acquisition pre-injection and 3, 15, and 90 min post-injection are colored with blue, red, green, and magenta, respectively. (E) shows a line plot with 95% CI of the continuous spectral timeline of deuterium signal for HDO (green) and [D_{15}]octanoate (pink) for 3 separate mice.

and 36 weeks compared to the mass at baseline (Figure 6A; Tables S6 and S7). Liver mass of fed mice was significantly increased after 8 weeks on HFD compared to baseline. By 17 weeks on HFD, liver mass increased profoundly from 1.22 ± 0.10 g at baseline to 3.45 ± 0.41 g and was significantly greater at 17, 24, and 36 weeks than that of the mice on normal chow at the same times (Figure 6A; Tables S6 and S7). The liver mass of fasted mice was unchanged throughout the experimental period for mice on the chow diet and at 8.5 weeks of HFD (Figure 6B). At 17, 24, and 36 weeks of HFD, the liver mass of fasted mice (2.76 ± 0.58 and 2.3 ± 0.77 g, respectively) was significantly higher than baseline (1.01 ± 0.05 g) or chow diet controls at 17, 24, and 36 weeks (1.36 ± 0.23 and 1.44 ± 0.28 g) (Figure 6B; Tables S6 and S7).

We determined both total hepatic β-oxidation and β-oxidation relative to liver mass (see STAR Methods for details; Figures 6C–6F; Table S6). From baseline through 24 weeks, neither total nor relative hepatic β-oxidation differed in mice with *ad libitum* access to normal chow (Figures 6C and 6E; Tables S6 and S7). In contrast, mice with *ad libitum* access to the HFD exhibited a significant increase in total β-oxidative capacity that coincided with the significant increase in liver mass at 17 and 24 weeks (Figures 6D, top, and 6A). However, when normalized for the increase in liver mass, the relative β-oxidative capacity for the HFD mice decreased at all time points compared to baseline (Figure 6D, bottom).

We found that fasted mice had reduced relative hepatic β-oxidation in mice on normal chow diet that was significant for the 17 and 36 week points compared to baseline (Figure 6E, bottom). At 8.5 weeks on the HFD and following overnight fasting, liver mass was the same as liver mass at the baseline of fasted mice (Figure 6A). However, livers of the fasted mice showed a significant reduction in both total and relative hepatic β-oxidative capacity at this time point (Figure 6E; Table S7). Like we observed for the fed state, livers from the fasting mice on the HFD at 17 and 24 weeks showed an increase in total hepatic β-oxidative capacity but decreased when normalized for the increase in liver size (Figure 6F). At 36 weeks on diet, an age-related decline of 20%–50% in total and relative β-oxidation was observed for the chow diet mice (Figures 6C and 6E). Conversely, the increase in total β-oxidation for HFD livers by 17 and 24 weeks was lost by 36 weeks, while relative β-oxidation continued to dramatically decline (Figures 6D and 6F; Tables S6 and S7). The time course indicates an increase followed by a collapse in compensatory total β-oxidation, while the efficiency (relative capacity) of octanoate oxidation declines as a function of the number of weeks on HFD.

To further assay liver metabolism in the context of MASLD, correlations of oxidative capacity and HDO production to known parameters associated with metabolic dysfunction were measured. When normalized to the metabolic associated steatosis (MAS) score, HFD animals had significantly lower values for both total and relative β-oxidative capacity in either the fed or fasted state (Figures 7A–7D). HDO production (Figures 7E–7H) was not well correlated with the MAS score in the fasted state, but in the fed state, it switched from a positive correlation for the total production to a negative correlation for the production/g liver, reinforcing the notion that octanoate oxidation decreases with accrued oxidative damage. Circulating ALT is often used as a marker of liver damage. Normalization of the oxidative

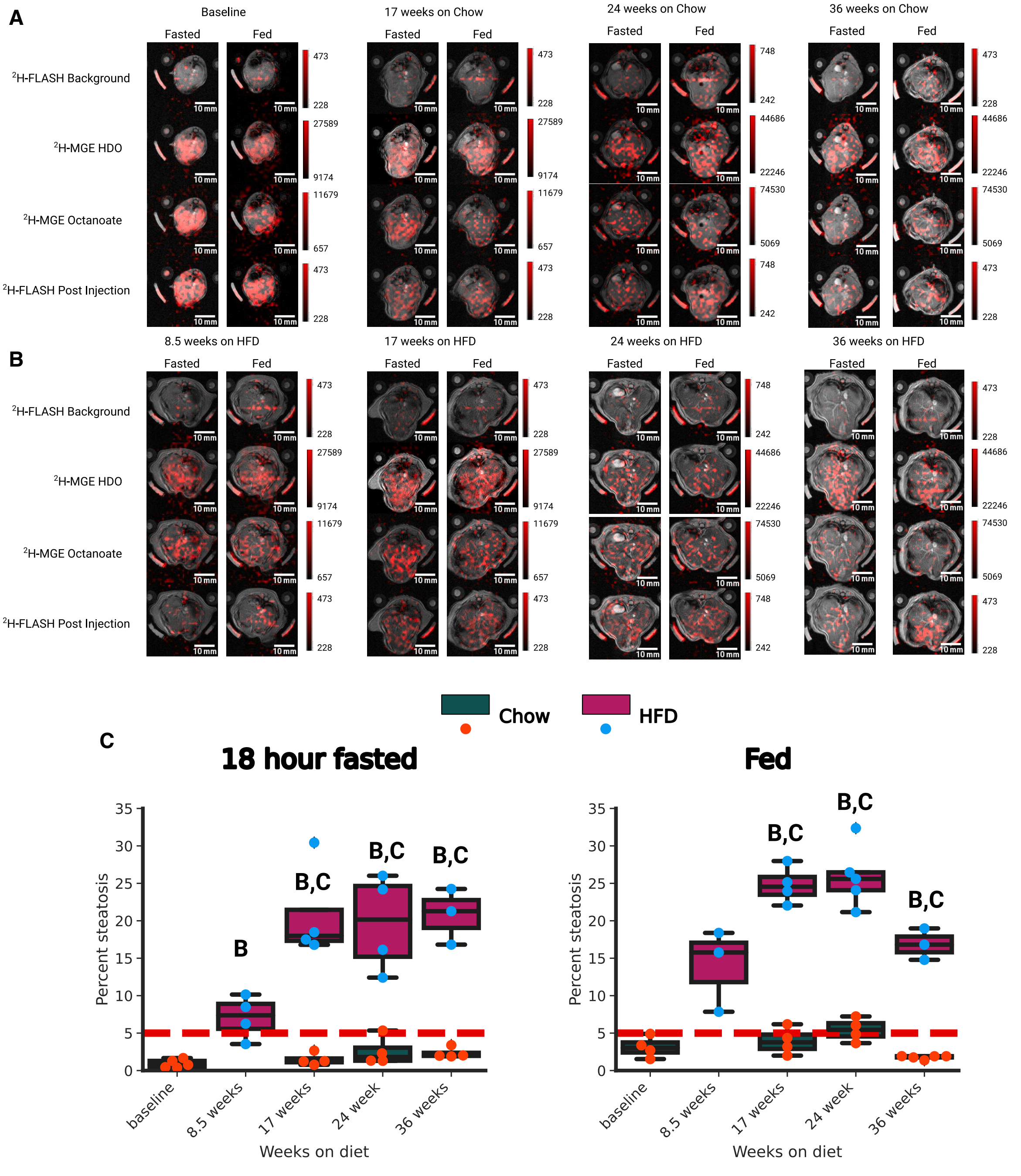

Figure 5. Representative metabolic imaging of C57BL/6J mouse liver for the dietary timeline from 8 to 44 weeks of age

(A and B) All images represent an overlay of the respective deuterium image with the proton axial for the hepatic region. Overlays are ordered from top to bottom per image as follows: ^{2}H-FLASH before injection of [D_{15}]octanoate, 27 min 2PD acquisition starting at 17 min post-injection (HDO and [D_{15}]octanoate components), and 27 min ^{2}H-FLASH acquisition starting at 62 min post-injection. For each given time point, the 18-h-fasted mice are in the left column, and the *ad-libitum*-fed mice are in the right column. Images were arranged with respect to timeline in the order of (A) baseline and 17, 24, and 36 weeks on chow diet and (B) 8.5, 17, 24, and 36 weeks on HFD.

(C) Percentage of steatosis score in 18-h-fasted (left) and *ad-libitum*-fed (right) C57BL/6J mice on either HFD (pink bar, blue dots) or chow diet (green bar, orange dots). The 5% steatosis cutoff for MASLD/NAFLD is represented as a red dashed bar.

Error bars represent the mean ± standard deviation. B refers to significance relative to baseline. C refers to significance when comparing the HFD mice to their chow diet counterparts for the same age. F refers to significance when comparing fed and fasted animals within the same diet and age. The numbers of fasted animals used were *n* = 5, 4, 4, 4, 4, 4, 3, and 4 at baseline, 8.5 weeks HFD, 17 weeks HFD, 17 weeks chow, 24 weeks HFD, 24 weeks chow, 36 weeks HFD, and 36 weeks chow, respectively. The numbers of fed animals used were *n* = 4, 3, 4, 4, 5, 4, 3, and 5 at baseline, 8.5 weeks HFD, 17 weeks HFD, 17 weeks chow, 24 weeks HFD, 24 weeks chow, 36 weeks HFD, and 36 weeks chow, respectively.

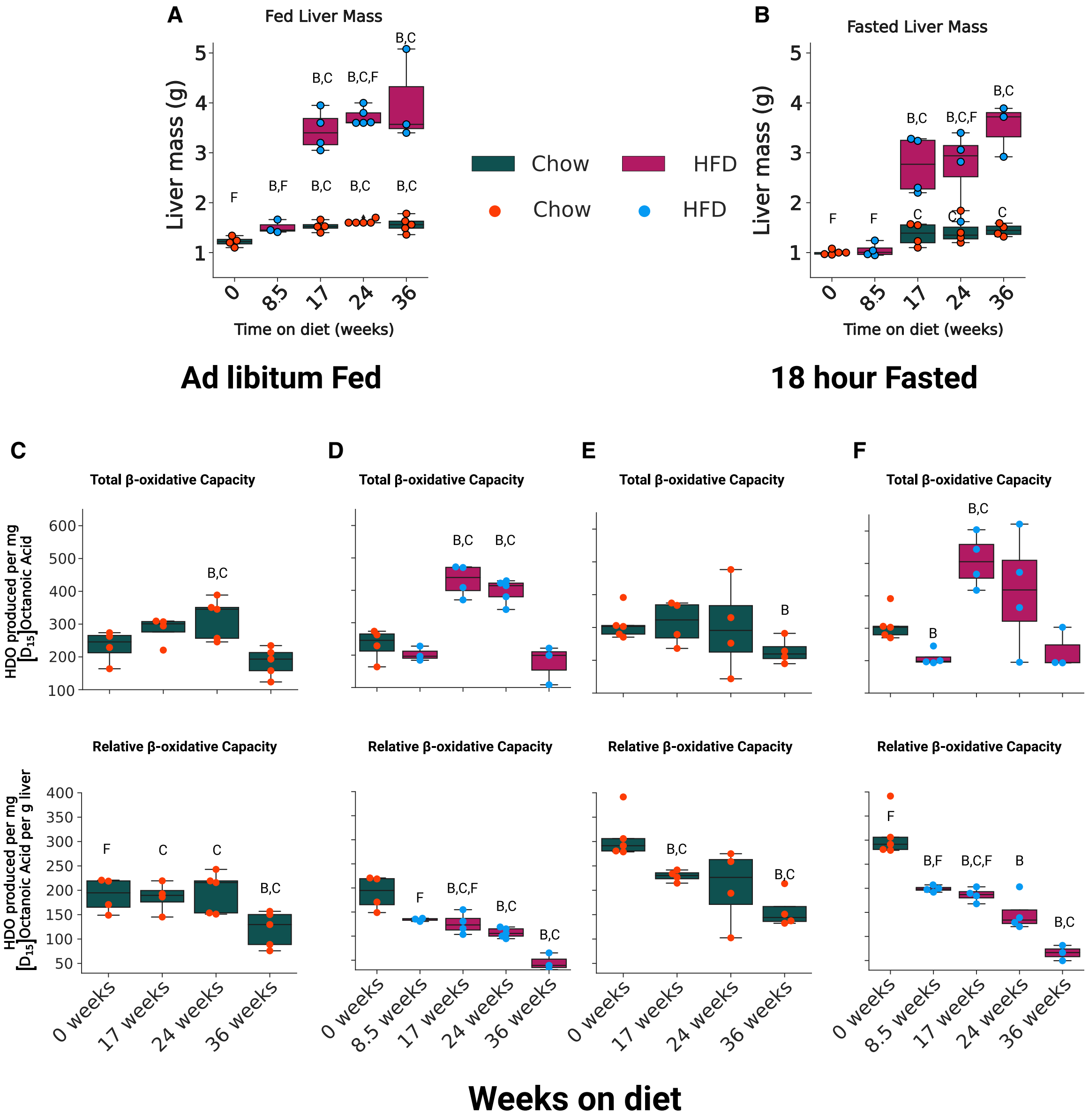

Figure 6. Quantitative measurements of liver mass as well as total hepatic β-oxidation and hepatic β-oxidation relative to liver mass

HFD-fed mice are in pink, while baseline and chow-fed mice are in dark green.

(A and B) Liver mass in grams from *ad libitum*-fed mice (*n* = 4, 3, 4, 4, 5, 5, 3, and 5 at baseline, 8.5 weeks HFD, 17 weeks HFD, 17 weeks chow, 24 weeks HFD, 24 weeks chow, 36 weeks HFD, and 36 weeks chow, respectively) (A) or 18-h-fasted mice that underwent deuterium MRI at the start of the diet (8 weeks of age) until the end of imaging (44 weeks of age) (*n* = 5, 4, 4, 4, 4, 4, 3, and 4 at baseline, 8.5 weeks HFD, 17 weeks HFD, 17 weeks chow, 24 weeks HFD, 24 weeks chow, 36 weeks HFD, and 36 weeks chow, respectively) (B). Weeks on diet was determined by access to the MRI system.

(C–F) MRI quantification of 2PD-derived HDO produced per mg of $[D_{15}]$octanoate injected (top) and HDO produced per mg of $[D_{15}]$octanoate and g of liver mass (bottom). See Table S7 for statistical evaluation. The quantification of liver images is ordered as follows: *ad-libitum*-fed mouse groups on (C) chow diet (*n* = 4, 4, 5, and 5 at 0, 17, 24, and 36 weeks of diet, respectively) or (D) HFD (*n* = 4, 3, 4, 5, and 3 at 0, 8.5, 17, 24, and 36 weeks of diet, respectively), followed by 18-h-fasted mouse groups on (E) chow diet (*n* = 5, 4, 4, and 4 at 0, 17, 24, and 36 weeks of diet, respectively) or (F) HFD (*n* = 5, 4, 4, 4, and 3 at 0, 8.5, 17, 24, and 36 weeks of diet, respectively).

Error bars represent the mean ± standard deviation. B refers to significance relative to baseline. C refers to significance when comparing the HFD mice to their chow diet counterparts for the same age. F refers to significance when comparing fed and fasted animals within the same diet and age.

capacity to ALT levels again produced a strong separation between the chow diet and HFD animals (Figures 7I–7L), with similar correlations in HDO production to those seen for the MAS score except with a stronger correlation for HFD, fasted animals between relative β-oxidative capacity and ALT (Figures 7M–7P).

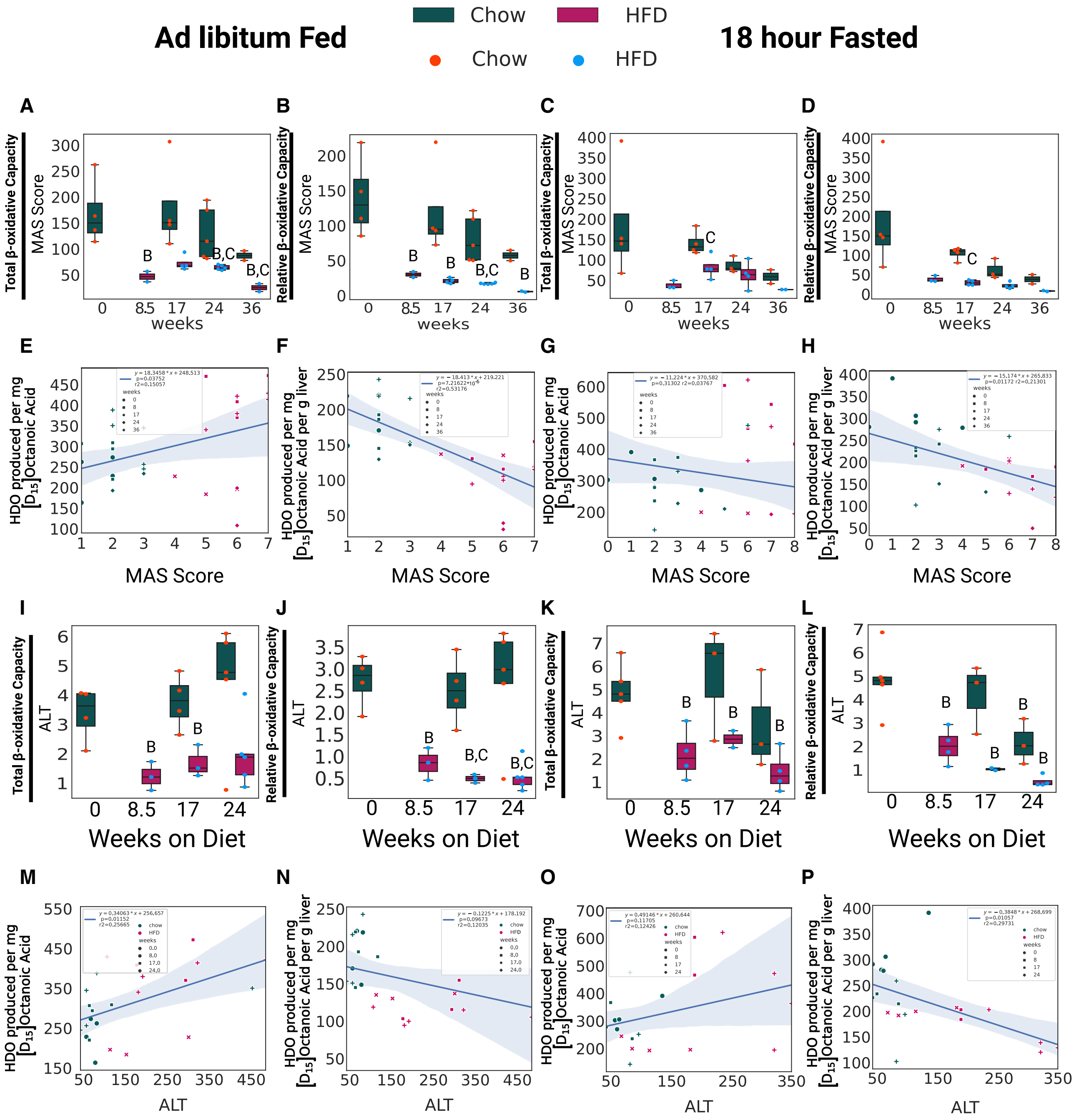

Figure 7. Correlation of HDO measures to histological score (MAS score) and liver inflammatory marker ALT during HFD

HFD fed mice are in pink, while baseline and chow fed mice are in dark green.

(A–D) Boxplot of (A) total β-oxidative capacity or (B) β-oxidative efficiency normalized to MAS score during diet timeline in *ad-libitum*-fed mice (*n* = 4, 2, 4, 4, 5, 5, 2, and 2 at baseline, 8.5 weeks on HFD, 17 weeks on HFD or chow, 24 weeks on HFD or chow, and 36 weeks on HFD or chow, respectively) or 18-h-fasted mice (C and D) (*n* = 4, 3, 4, 4, 3, 4, 2, and 2 at baseline, 8.5 weeks on HFD, 17 weeks on HFD or chow, 24 weeks on HFD or chow, and 36 weeks on HFD or chow, respectively).

(E–H) Correlation plot with shaded area represented 95% CI of (E) total β-oxidative capacity or (F) β-oxidative efficiency to MAS score during diet timeline in *ad-libitum*-fed mice or 18-h-fasted mice (G and H).

(I–L) Boxplot of total (I) or relative (J) β-oxidative capacity normalized to ALT score during diet timeline in *ad-libitum*-fed mice (*n* = 4, 3, 3, 4, 3, 5, and 5 at baseline, 8.5 weeks on HFD, 17 weeks on HFD or chow, and 24 weeks on HFD or chow, respectively) or 18-h-fasted mice (*n* = 5, 4, 3, 2, 3, and 4 at baseline, 8.5 weeks on HFD, 17 weeks on HFD or chow, and 24 weeks on HFD or chow, respectively) (K and L).

(legend continued on next page)

DISCUSSION

DMR of the perfused liver

Imaging hepatic energy metabolism is not an easily achieved goal because positron emission tomography (PET) methods depend upon access to a cyclotron for production of ^{11}C or ^{18}F, and MR-based methods, to date, have used single-voxel spectroscopy with administration of a large, limiting quantity of ^{13}C-labeled substrate. We postulated that imaging with DMR could provide metabolic contrast in a more accessible paradigm than either the PET or previous MR approaches. We first assessed the capacity of monitoring HDO production with DMR to identify changes in β-oxidation for perfused livers. Using a perfused liver model, we removed contributions from extraneous tissues, and our results were solely indicative of hepatic metabolism. The $[D_{15}]$octanoate substrate used for the *ex-vivo*-perfused liver experiments generated a quantifiable measure of β-oxidation through the production of HDO (Figures 2C–2E and 2F).[21,22,29] NMR approaches of this nature are quantitative and revealed that β-oxidation was decreased per gram of liver protein in the HFD mice, which was confirmed by independent direct measurements of $[D_{15}]$octanoate consumption by GC-MS analysis of perfusate (Figures 2G and 2H). Clearance of $[D_{15}]$octanoate from the perfusate is a similar measure to ^{13}C tracer turnover measurements during *in vivo* assessment of lipid metabolism in patients with MASLD/NAFLD.[30–36]

Another common method for inferring β-oxidation with hepatic specificity is the measurement of labeled ketones after tracer administration.[37] β-Oxidation produces acetyl-CoA that is required to make ketones (Figure S1; Table S1), and the liver is considered the primary source of ketogenesis.[38] Because there was no difference in ketone isotopic labeling pattern for the HFD and LFD groups, we compared the total ketone output (Figure 3C). However, if we had relied on the commonly used metric of ketogenic output alone to determine oxidative rates from the liver, our results would indicate either higher total oxidative potential or no relative difference between dietary states (Figures 2G and 2H).[17–19] In the perfusion model, where the liver is the only organ, the $[D_{15}]$octanoate consumption from perfusate is a more accurate proxy for β-oxidation than the downstream pathway of ketogenesis and is in complete alignment with our HDO measure by DMR. DMR of HDO produced from deuterated fatty acids, therefore, bypasses the inherent limitations of less direct β-oxidation measurements.

A limited set of equations modeling only octanoate consumption and HDO production in the perfused liver would produce estimates of β-oxidation with low accuracy due to the uncertainties associated with the multiple pathways converging at acetyl-CoA. A more complete INCA model of central metabolism considerably reduced the error in rate assessments.[39] Our enhanced INCA model of perfused liver metabolism used HDO production, O_2 consumption, ketone production, pool sizes, and enrichments of multiple metabolites. In addition to validating the claims from our DMR method, we also determined that a decrease in $FADH_2$ oxidation in the HFD mouse liver occurred, which has been previously observed in models of β-oxidative decline with isolated mitochondria.[40] NADH turnover trended lower, but the lack of significant differences for NADH turnover is likely related to the difference in model variability associated with $FADH_2$ metabolism (two reactions) vs. NADH in 8 reactions (Table S1; Figures 3D and 3E). The rate estimates from the INCA model also showed significant increases in total β-oxidation and $FADH_2$ oxidation for HFD livers, which was in line with the ^{11}C palmitate PET analysis of oxidative byproducts and isolated mitochondria experiments.[41] These observations support the robustness of using DMR to assess changes in fatty acid oxidative metabolism post-injection of $[D_{15}]$octanoate by monitoring HDO. In conjunction with the decreased HDO production rate per gram of liver protein, these results indicated a possible defect in β-oxidative efficiency caused by deleterious effects of the HFD, which is consistent with a 16 week HFD study with C57BL/6J mice that showed reduced transcripts for LCAD and medium-chain acyl-CoA dehydrogenase (MCAD).[18] Here, *LCAD* expression was insignificantly lower for HFD livers, and western blot analysis showed that protein abundance was unchanged compared with livers from LFD mice (Figure S5). This difference in LCAD results with those in the previous study[18] may relate to the greater weight gain exhibited by the HFD animals in our study, which were heavier by 15%, suggesting that the stage of MASLD was more advanced and the mice had accrued greater damage to the hepatocytes than previously.[18] To further confirm increased β-oxidation as the mechanism underlying increased HDO production, we performed separate experiments using glucagon to upregulate fatty acid metabolism.[42,43]

Unlike the previously used tracer methods based on MR detection, octanoate induces β-oxidation and ketogenesis[17–19,36,37,41,44–48] and is oxidized in the hepatocyte without the need for CPT-I activity.[25] As a direct consequence of the higher β-oxidation in our system, octanoate β-oxidation represented a majority of the oxidative metabolism, suppressing the TCA cycle's contribution (Figures 3D and 3E). Emphasis on β-oxidation by this approach is a potential source of differences to other measures of total oxidative metabolism in rodent MASLD models but may aid in identifying perturbations in the β-oxidative pathway specifically and help assess the severity of steatohepatitis, MASLD progression, and eventually, response to pharmacological interventions.

Imaging hepatic oxidative flux

Using HDO as a readout of hepatic β-oxidation has distinct advantages. HDO can be directly imaged, unlike thermally polarized ^{13}C methods, which are restricted to a single voxel covering the whole liver in humans. Additionally, based on studies in isolated mitochondria, HDO is retained in hepatic mitochondria post-$[D_{15}]$octanoate incubation for at least an hour (Figure S10;

(M–P) Correlation plot with shaded area represents 95% CI of (M) total β-oxidative capacity or (N) β-oxidative efficiency to MAS score during diet timeline in *ad-libitum*-fed mice or 18-h-fasted mice (O and P). See Table S7 for statistical evaluation.

Error bars represent the mean ± standard deviation. B refers to significance relative to baseline. C refers to significance when comparing the HFD mice to their chow diet counterparts for the same age.

see star methods). Retention of HDO in liver mitochondria on this timescale suggests that our estimates of hepatic β-oxidation *in vivo* are organ specific. When performing deuterium metabolic imaging, we observed the highest signal in the liver for axial and coronal images relative to the kidneys, heart, and shoulder muscle (Figures 4A–4C). $[D_{15}]$octanoate was clearly used as an oxidative substrate, as evidenced by the rapid increase in HDO pool size detected by deuterium spectroscopy of the torso and 2PD imaging of the liver (Figures 4A, 4D, and 4E). Various characteristics of the liver, such as its fenestrated blood vessels, proximity to the heart after tail vein injection, mitochondrial abundance, and physical size, support its major role in β-oxidative metabolism. These characteristics lead us to the conclusion that our *in vivo* estimates of hepatic β-oxidation are organ specific without deleterious contribution from other tissues. Additionally, $[D_{15}]$octanoate is oxidized in the liver in a CPT1- and CPT2-independent manner, unlike in mitochondria from skeletal muscle or cardiac muscle.[25]

Deuterium metabolic images at 8, 17, 24, and 36 weeks of HFD showed a high degree of signal localization to the liver after injection of $[D_{15}]$octanoate (Figure 5). Before injection of $[D_{15}]$octanoate, body noise was very low, and the external reference phantoms are the primary component visible in the ^{2}H-FLASH images (Figure 5). Less signal from the octanoate component in 2PD was observed in the fed compared to the fasted animals (Figure 5). The signal differences suggested that lower amounts of $[D_{15}]$octanoate were taken up by the liver in the fed state, which may contribute to the higher total and relative β-oxidation observed in the fasted animals at multiple time points (Figure 5). As animal size (and age) increased, the distribution of the deuterium signal over the liver post-injection became less uniform (Figure 5). The decrease in uniform signal indicated changes in HDO production through less β-oxidative activity, differences in zonation, reduced transport of $[D_{15}]$octanoate, or a combination thereof throughout the liver. This effect was also observed in the decrease of relative β-oxidation as the HFD progressed (Figures 6C–6F, bottom row; Tables S6 and S7).

Throughout the course of the HFD, relative β-oxidation decreased most dramatically within the first 8 weeks of HFD and continued to decline in the latter weeks of diet (Figures 6D and 6F, bottom row). The decrease in relative β-oxidation occurred before major increases in liver mass and total β-oxidation (Figures 6A, 6B, 6D, and 6F, top row). The increase in the percentage of steatosis by histological assessment to MASLD status for HFD animals alone occurred by 8 weeks of HFD (Figures S7 and S8). The timeline implied that excess lipids and higher caloric intake in the HFD animals led to a decrement in liver β-oxidative capacity before major changes in hepatic structure toward hepatomegaly and greater total hepatic β-oxidation occurred. Unlike HFD animals, chow diet animals did not have a significant increase in total β-oxidation (Figures 6C and 6E, top row). A small decrement in relative β-oxidation for overnight-fasted, chow diet animals was observed at 17 and 36 weeks of diet only (Figure 6E, bottom row). HDO production and oxidative capacity in general displayed strong dependencies on both the MAS score and circulating ALT (Figures 7 and S9). Total HDO production and oxidative capacity correlate positively with ALT and MAS score, but the trends reversed when normalized values of HDO and oxidative capacity were used. These observations support our hypothesis that $[D_{15}]$octanoate MRI can assess liver function *in vivo* in an accurate manner. Furthermore, the kinetic profile for HDO production in the perfused liver and *in vivo* shared the same bimodal response, indicating the dominance of the liver for overall HDO production (Figures 2E and 4E). Therefore, DMRI after injection of $[D_{15}]$octanoate is a powerful tool for assessing hepatic β-oxidation directly, with a limited contribution from TCA cycle metabolism. Although octanoate administration downregulates TCA cycle turnover, we propose that the metric of β-oxidation produced by these methods can generate insights into dysregulated hepatic metabolism, such as those induced by HFD. Because DMRI is already practiced in humans with deuterated glucose, this approach should be readily translated to human studies.

Limitations of the study

Our data are acquired at a field strength of 11.1 T, which results in clearly defined water and fatty acid peaks, enabling the use of simple 2PD methods for metabolic imaging. At the commonly used clinical field strength of 3 T, the separation would not be as large and would require either chemical shift imaging or a multi-echo approach to achieve chemical separation. Other dietary models of MASLD/MASH might cause differential changes in octanoate oxidation. The contrast agent $[D_{15}]$octanoate is approximately twice the cost of $[6,6'\text{-}D_2]$glucose (~$340/g vs. ~$180/g); however, we have used concentrations 1/3–1/6 that of typical glucose-based imaging paradigms. It is not clear what dosage would be suitable for application in humans.

Conclusion

We demonstrated that HDO production from deuterated fatty acids is a viable methodology for estimating functional differences in the rate of hepatic β-oxidation in a diet-induced model of MASLD. β-Oxidation inactivity has been cited as a contributor to excess fatty acids that drive ER stress and lipoapoptosis.[14–16] Conversely, increased β-oxidation, in a high fatty acid environment during MASLD, acts as a direct contributor to the overactive production of inflammatory molecules such as ROS.[17–19,41] We directly measured hepatic β-oxidation *ex vivo and in vivo* with DMR of hepatic deuterated fatty acid metabolism in a MASLD model (Figures 2D, 2E, 2F, 2H, 3D, 3E, and 6C–6F). Our results suggested that both views of fatty acid oxidation are valid. Whole-liver fatty acid metabolism is transiently increased in this model, but the oxidative process is less efficient in the diseased liver at all time points. We surmise that hepatomegaly is a compensatory response to the increased availability of calories on HFD, but the proliferation of hepatocytes is counterbalanced by the eventual loss of efficiency in the oxidative pathway. The sensitivity of this methodology, which is inherently non-invasive, provides an alternative route for new paradigms of clinical assessment for MASLD diagnosis, monitoring, and treatment. The $[U\text{-}^{13}C]$octanoate breath test used extensively in humans has shown a predictive ability for the presence of MASLD/MASH[49] as well as its staging.[50] We envision a future where DMRI and related techniques will allow a precision assessment of metabolic dysfunction in MASLD, the severity of steatohepatitis and disease stage, and progression and response to pharmacological interventions.

RESOURCE AVAILABILITY

Lead contact

Further information and requests for resources and reagents should be directed to and will be fulfilled by the lead contact, Matthew E. Merritt (mathewmerritt@ufl.edu).

Materials availability

This study did not generate new unique reagents.

Data and code availability

- **Data:** All data required to understand the findings of this study are provided in the main manuscript or the supplementary material.
- **Code:** All the code used in this study is readily available to general users of the softwares reported.
- **General Statement:** Any additional information required to reanalyze the data reported in this paper is available from the lead contact upon request.

ACKNOWLEDGMENTS

M.E.M. acknowledges support from National Institutes of Health grants R01-DK132254 and R01-EB032376. J.A.B. acknowledges the support of R01-EB032376. N.E.S. acknowledges the support of R01-DK112865. A portion of this work was performed in the McKnight Brain Institute at the National High Magnetic Field Laboratory's Advanced Magnetic Resonance Imaging and Spectroscopy (AMRIS) Facility, which is supported by National Science Foundation Cooperative Agreement DMR-2128556 and the state of Florida.

AUTHOR CONTRIBUTIONS

Conceptualization, M.M., M.R., J.A.B., and M.E.M.; methodology, M.M., M.C.C., A.R., M.R., R.M., G.S., A.B., A.G., M.E.G., V.R.M., and D.G.; formal analysis, M.M., M.C.C., A.R., M.R., G.S., A.B., V.R.M., and D.G.; data curation, M.M., M.C.C., A.R., M.R., G.S., A.B., V.R.M., and D.G.; investigation, M.M., M.C.C., A.R., M.R., R.M., G.S., A.B., A.G., M.G., V.R.M., D.G., N.E.S., J.A.B., K.C., and M.E.M.; resources, N.E.S., J.A.B., K.C., and M.E.M.; writing – original draft, M.M., M.R., and M.E.M.; writing – review & editing, M.M., M.C.C., A.R., M.R., R.M., G.S., A.B., A.G., M.G., V.R.M., D.G., N.E.S., J.A.B., K.C., and M.E.M.; supervision, N.E.S., J.A.B., K.C., and M.E.M.; funding acquisition, N.E.S. and M.E.M.

DECLARATION OF INTERESTS

M.E.M. and R.M. are holders of patent ##T17984US002 related to metabolic imaging of HDO.

STAR★METHODS

Detailed methods are provided in the online version of this paper and include the following:

- KEY RESOURCES TABLE
- EXPERIMENTAL MODEL AND STUDY PARTICIPANT DETAILS
  - ○ Animals
- METHOD DETAILS
  - ○ Liver perfusion
  - ○ NMR spectroscopy
  - ○ Gas chromatography – Mass spectrometry
  - ○ MTBSTFA derivatization
  - ○ Aldonitrile pentapropionate derivatization
  - ○ Protein estimation in liver tissue
  - ○ Expression profiles in liver tissue
  - ○ Mitochondrial isolation to determine HDO retention
  - ○ Deuterium magnetic resonance imaging
  - ○ Localization of HDO to the mitochondrial compartment
  - ○ Histological assessment of steatosis in diet mice
  - ○ Liver triglyceride assay
  - ○ Immunofluorescence
  - ○ ALT and AST
- QUANTIFICATION AND STATISTICAL ANALYSIS
  - ○ Metabolite analysis by GC-MS
  - ○ Peak integration
  - ○ Isotopic ratio and fractional enrichment
  - ○ INCA metabolic modeling
  - ○ Deuterium magnetic resonance imaging
  - ○ Statistical analysis
  - ○ Software

SUPPLEMENTAL INFORMATION

Supplemental information can be found online at https://doi.org/10.1016/j.xcrm.2024.101714.

Received: September 1, 2023
Revised: July 16, 2024
Accepted: August 13, 2024
Published: September 5, 2024

REFERENCES

1. Cusi, K., Isaacs, S., Barb, D., Basu, R., Caprio, S., Garvey, W.T., Kashyap, S., Mechanick, J.I., Mouzaki, M., Nadolsky, K., et al. (2022). American Association of Clinical Endocrinology Clinical Practice Guideline for the Diagnosis and Management of Nonalcoholic Fatty Liver Disease in Primary Care and Endocrinology Clinical Settings. Endocr. Pract. *28*, 528–562. https://doi.org/10.1016/j.eprac.2022.03.010.
2. Rinella, M.E., Neuschwander-Tetri, B.A., Siddiqui, M.S., Abdelmalek, M.F., Caldwell, S., Barb, D., Kleiner, D.E., and Loomba, R. (2023). AASLD Practice Guidance on the clinical assessment and management of nonalcoholic fatty liver disease. Hepatology *77*, 1797–1835. https://doi.org/10.1097/HEP.0000000000000323.
3. Younossi, Z.M., and Henry, L. (2024). Understanding the Burden of Nonalcoholic Fatty Liver Disease: Time for Action. Diabetes Spectr. *37*, 9–19. https://doi.org/10.2337/dsi23-0010.
4. Rinella, M.E., Lazarus, J.V., Ratziu, V., Francque, S.M., Sanyal, A.J., Kanwal, F., Romero, D., Abdelmalek, M.F., Anstee, Q.M., Arab, J.P., et al. (2023). A multisociety Delphi consensus statement on new fatty liver disease nomenclature. Hepatology *78*, 1966–1986.
5. Bril, F., Sanyal, A., and Cusi, K. (2023). Metabolic Syndrome and Its Association with Nonalcoholic Steatohepatitis. Clin. Liver Dis. *27*, 187–210. https://doi.org/10.1016/j.cld.2023.01.002.
6. Nogueira, J.P., and Cusi, K. (2024). Role of Insulin Resistance in the Development of Nonalcoholic Fatty Liver Disease in People With Type 2 Diabetes: From Bench to Patient Care. Diabetes Spectr. *37*, 20–28. https://doi.org/10.2337/dsi23-0013.
7. Younossi, Z.M., Stepanova, M., Ong, J., Trimble, G., AlQahtani, S., Younossi, I., Ahmed, A., Racila, A., and Henry, L. (2021). Nonalcoholic Steatohepatitis Is the Most Rapidly Increasing Indication for Liver Transplantation in the United States. Clin. Gastroenterol. Hepatol. *19*, 580–589.e5. https://doi.org/10.1016/j.cgh.2020.05.064.
8. Golabi, P., Paik, J.M., Kumar, A., Al Shabeeb, R., Eberly, K.E., Cusi, K., GunduRao, N., and Younossi, Z.M. (2023). Nonalcoholic fatty liver disease (NAFLD) and associated mortality in individuals with type 2 diabetes, prediabetes, metabolically unhealthy, and metabolically healthy individuals in the United States. Metabolism *146*, 155642. https://doi.org/10.1016/j.metabol.2023.155642.
9. Harrison, S.A., Gawrieh, S., Roberts, K., Lisanti, C.J., Schwope, R.B., Cebe, K.M., Paradis, V., Bedossa, P., Aldridge Whitehead, J.M., Labourdette, A.,

et al. (2021). Prospective evaluation of the prevalence of non-alcoholic fatty liver disease and steatohepatitis in a large middle-aged US cohort. J. Hepatol. *75*, 284–291. https://doi.org/10.1016/j.jhep.2021.02.034.

10. American Diabetes Association Professional Practice; ElSayed, N.A., Aleppo, G., Bannuru, R.R., Bruemmer, D., Collins, B.S., Cusi, K., Ekhlaspour, L., Fleming, T.K., Hilliard, M.E., et al. (2024). 4. Comprehensive Medical Evaluation and Assessment of Comorbidities: <i>Standards of Care in Diabetes—2024</i&gt. Diabetes Care *47*, S52–S76. https://doi.org/10.2337/dc24-S004.
11. Genua, I., and Cusi, K. (2024). Pharmacological Approaches to Nonalcoholic Fatty Liver Disease: Current and Future Therapies. Diabetes Spectr. *37*, 48–58. https://doi.org/10.2337/dsi23-0012.
12. Cusi, K. (2024). Selective Agonists of Thyroid Hormone Receptor Beta for the Treatment of NASH. N. Engl. J. Med. *390*, 559–561. https://doi.org/10.1056/NEJMe2314365.
13. Harrison, S.A., Bedossa, P., Guy, C.D., Schattenberg, J.M., Loomba, R., Taub, R., Labriola, D., Moussa, S.E., Neff, G.W., Rinella, M.E., et al. (2024). A Phase 3, Randomized, Controlled Trial of Resmetirom in NASH with Liver Fibrosis. N. Engl. J. Med. *390*, 497–509. https://doi.org/10.1056/NEJMoa2309000.
14. Pilar Valdecantos, M., Prieto-Hontoria, P.L., Pardo, V., Módol, T., Santamaría, B., Weber, M., Herrero, L., Serra, D., Muntané, J., Cuadrado, A., et al. (2015). Essential role of Nrf2 in the protective effect of lipoic acid against lipoapoptosis in hepatocytes. Free Radic. Biol. Med. *84*, 263–278. https://doi.org/10.1016/j.freeradbiomed.2015.03.019.
15. Unger, R.H., and Orci, L. (2002). Lipoapoptosis: its mechanism and its diseases. Biochim. Biophys. Acta *1585*, 202–212. https://doi.org/10.1016/S1388-1981(02)00342-6.
16. Petersen, K.F., Befroy, D.E., Dufour, S., Rothman, D.L., and Shulman, G.I. (2016). Assessment of Hepatic Mitochondrial Oxidation and Pyruvate Cycling in NAFLD by 13C Magnetic Resonance Spectroscopy. Cell Metabol. *24*, 167–171. https://doi.org/10.1016/j.cmet.2016.06.005.
17. Fletcher, J.A., Deja, S., Satapati, S., Fu, X., Burgess, S.C., and Browning, J.D. (2019). Impaired ketogenesis and increased acetyl-CoA oxidation promote hyperglycemia in human fatty liver. JCI Insight *5*, e127737. https://doi.org/10.1172/jci.insight.127737.
18. Muyyarikkandy, M.S., McLeod, M., Maguire, M., Mahar, R., Kattapuram, N., Zhang, C., Surugihalli, C., Muralidaran, V., Vavilikolanu, K., Mathews, C.E., et al. (2020). Branched chain amino acids and carbohydrate restriction exacerbate ketogenesis and hepatic mitochondrial oxidative dysfunction during NAFLD. Faseb. J. *34*, 14832–14849. https://doi.org/10.1096/fj.202001495R.
19. Sunny, N.E., Parks, E.J., Browning, J.D., and Burgess, S.C. (2011). Excessive Hepatic Mitochondrial TCA Cycle and Gluconeogenesis in Humans with Nonalcoholic Fatty Liver Disease. Cell Metabol. *14*, 804–810. https://doi.org/10.1016/j.cmet.2011.11.004.
20. Yuzefovych, L.V., Solodushko, V.A., Wilson, G.L., and Rachek, L.I. (2012). Protection from Palmitate-Induced Mitochondrial DNA Damage Prevents from Mitochondrial Oxidative Stress, Mitochondrial Dysfunction, Apoptosis, and Impaired Insulin Signaling in Rat L6 Skeletal Muscle Cells. Endocrinology *153*, 92–100. https://doi.org/10.1210/en.2011-1442.
21. Mahsut, A., Wang, S.-P., McLaren, D.G., Bhat, G., Herath, K., Miller, P.L., Hubbard, B.K., Johns, D.G., Previs, S.F., and Roddy, T.P. (2011). Headspace analyses of 2H labeling of acetone: Enabling studies of fatty acid oxidation in vivo. Anal. Biochem. *408*, 351–353. https://doi.org/10.1016/j.ab.2010.09.016.
22. Mahar, R., Zeng, H., Giacalone, A., Ragavan, M., Mareci, T.H., and Merritt, M.E. (2021). Deuterated water imaging of the rat brain following metabolism of [^{2}H $_{7}$]glucose. Magn. Reson. Med. *85*, 3049–3059. https://doi.org/10.1002/mrm.28700.
23. Delgado, T.C., Pinheiro, D., Caldeira, M., Castro, M.M.C.A., Geraldes, C.F.G.C., López-Larrubia, P., Cerdán, S., and Jones, J.G. (2009). Sources of hepatic triglyceride accumulation during high-fat feeding in the healthy rat. NMR Biomed. *22*, 310–317. https://doi.org/10.1002/nbm.1327.
24. Houten, S.M., and Wanders, R.J.A. (2010). A general introduction to the biochemistry of mitochondrial fatty acid β-oxidation. J. Inherit. Metab. Dis. *33*, 469–477. https://doi.org/10.1007/s10545-010-9061-2.
25. Pereyra, A.S., Harris, K.L., Soepriatna, A.H., Waterbury, Q.A., Bharathi, S.S., Zhang, Y., Fisher-Wellman, K.H., Goergen, C.J., Goetzman, E.S., and Ellis, J.M. (2021). Octanoate is differentially metabolized in liver and muscle and fails to rescue cardiomyopathy in CPT2 deficiency. J. Lipid Res. *62*, 100069. https://doi.org/10.1016/j.jlr.2021.100069.
26. McGarry, J.D., and Foster, D.W. (1971). The Regulation of Ketogenesis from Octanoic Acid. J. Biol. Chem. *246*, 1149–1159. https://doi.org/10.1016/S0021-9258(18)62443-3.
27. Berglund, M., and Wieser, M.E. (2011). Isotopic compositions of the elements 2009 (IUPAC Technical Report). Pure Appl. Chem. *83*, 397–410. https://doi.org/10.1351/PAC-REP-10-06-02.
28. Rahim, M., Ragavan, M., Deja, S., Merritt, M.E., Burgess, S.C., and Young, J.D. (2022). INCA 2.0: A tool for integrated, dynamic modeling of NMR- and MS-based isotopomer measurements and rigorous metabolic flux analysis. Metab. Eng. *69*, 275–285. https://doi.org/10.1016/j.ymben.2021.12.009.
29. Mahar, R., Donabedian, P.L., and Merritt, M.E. (2020). HDO production from [2H7]glucose Quantitatively Identifies Warburg Metabolism. Sci. Rep. *10*, 8885. https://doi.org/10.1038/s41598-020-65839-8.
30. Eaton, R.P., Berman, M., and Steinberg, D. (1969). Kinetic studies of plasma free fatty acid and triglyceride metabolism in man. J. Clin. Invest. *48*, 1560–1579. https://doi.org/10.1172/JCI106122.
31. Guo, Z., Nielsen, S., Burguera, B., and Jensen, M.D. (1997). Free fatty acid turnover measured using ultralow doses of [U-13C]palmitate. J. Lipid Res. *38*, 1888–1895. https://doi.org/10.1016/S0022-2275(20)37163-7.
32. Horowitz, J.F., Coppack, S.W., Paramore, D., Cryer, P.E., Zhao, G., and Klein, S. (1999). Effect of short-term fasting on lipid kinetics in lean and obese women. Am. J. Physiol. *276*, E278–E284. https://doi.org/10.1152/ajpendo.1999.276.2.E278.
33. Klein, S., Coyle, E.F., and Wolfe, R.R. (1994). Fat metabolism during low-intensity exercise in endurance-trained and untrained men. Am. J. Physiol. *267*, E934–E940. https://doi.org/10.1152/ajpendo.1994.267.6.E934.
34. Magkos, F., and Mittendorfer, B. (2009). Stable isotope-labeled tracers for the investigation of fatty acid and triglyceride metabolism in humans <i>in vivo</i&gt. Clin. Lipidol. *4*, 215–230. https://doi.org/10.2217/clp.09.9.
35. Teusink, B., Voshol, P.J., Dahlmans, V.E.H., Rensen, P.C.N., Pijl, H., Romijn, J.A., and Havekes, L.M. (2003). Contribution of Fatty Acids Released From Lipolysis of Plasma Triglycerides to Total Plasma Fatty Acid Flux and Tissue-Specific Fatty Acid Uptake. Diabetes *52*, 614–620. https://doi.org/10.2337/diabetes.52.3.614.
36. Wolfe, R.R., Evans, J.E., Mullany, C.J., and Burke, J.F. (1980). Measurement of plasma free fatty acid turnover and oxidation using [1-13C]palmitic acid. Biomed. Mass Spectrom. *7*, 168–171. https://doi.org/10.1002/bms.1200070407.
37. Yeh, Y.-Y., and Zee, P. (1976). Relation of Ketosis to Metabolic Changes Induced by Acute Medium-Chain Triglyceride Feeding in Rats. J. Nutr. *106*, 58–67. https://doi.org/10.1093/jn/106.1.58.
38. McGarry, J.D., and Foster, D.W. (1969). Ketogenesis and Cholesterol Synthesis in Normal and Neoplastic Tissues of the Rat. J. Biol. Chem. *244*, 4251–4256. https://doi.org/10.1016/S0021-9258(17)36409-8.
39. Young, J.D. (2014). INCA: a computational platform for isotopically nonstationary metabolic flux analysis. Bioinformatics *30*, 1333–1335. https://doi.org/10.1093/bioinformatics/btu015.
40. Koves, T.R., Zhang, G.-F., Davidson, M.T., Chaves, A.B., Crown, S.B., Johnson, J.M., Slentz, D.H., Grimsrud, P.A., and Muoio, D.M. (2023). Pyruvate-supported flux through medium-chain ketothiolase promotes mitochondrial lipid tolerance in cardiac and skeletal muscles. Cell Metabol. *35*, 1038–1056.e8. https://doi.org/10.1016/j.cmet.2023.03.016.

41. Han, Q., Cao, Y., Gathaiya, N., Kemp, B.J., and Jensen, M.D. (2018). Free fatty acid flux measured using [1- ^{11} C]palmitate positron emission tomography and [U- ^{13} C]palmitate in humans. Am. J. Physiol. Endocrinol. Metab. *314*, E413–E417. https://doi.org/10.1152/ajpendo.00284.2017.

42. Heimberg, M., Weinstein, I., and Kohout, M. (1969). The effects of glucagon, dibutyryl cyclic adenosine 3', 5'-monophosphate, and concentration of free fatty acid on hepatic lipid metabolism. J. Biol. Chem. *244*, 5131–5139.

43. Longuet, C., Sinclair, E.M., Maida, A., Baggio, L.L., Maziarz, M., Charron, M.J., and Drucker, D.J. (2008). The glucagon receptor is required for the adaptive metabolic response to fasting. Cell Metabol. *8*, 359–371.

44. Koutsari, C., Ali, A.H., Mundi, M.S., and Jensen, M.D. (2013). Measuring plasma fatty acid oxidation with intravenous bolus injection of 3H- and 14C-fatty acid. J. Lipid Res. *54*, 254–264. https://doi.org/10.1194/jlr.P031153.

45. Koutsari, C., and Jensen, M.D. (2006). Thematic review series: Patient-Oriented Research. Free fatty acid metabolism in human obesity. J. Lipid Res. *47*, 1643–1650. https://doi.org/10.1194/jlr.R600011-JLR200.

46. McCullough, A., Previs, S., and Kasumov, T. (2018). Stable isotope-based flux studies in nonalcoholic fatty liver disease. Pharmacol. Ther. *181*, 22–33. https://doi.org/10.1016/j.pharmthera.2017.07.008.

47. Previs, S.F., McLaren, D.G., Wang, S.-P., Stout, S.J., Zhou, H., Herath, K., Shah, V., Miller, P.L., Wilsie, L., Castro-Perez, J., et al. (2014). New methodologies for studying lipid synthesis and turnover: Looking backwards to enable moving forwards. Biochim. Biophys. Acta *1842*, 402–413. https://doi.org/10.1016/j.bbadis.2013.05.019.

48. Sidossis, L.S., Coggan, A.R., Gastaldelli, A., and Wolfe, R.R. (1995). A new correction factor for use in tracer estimations of plasma fatty acid oxidation. Am. J. Physiol. *269*, E649–E656. https://doi.org/10.1152/ajpendo.1995.269.4.E649.

49. Mucinski, J.M., Perry, A.M., Fordham, T.M., Diaz-Arias, A., Ibdah, J.A., Rector, R.S., and Parks, E.J. (2023). Labeled breath tests in patients with NASH: Octanoate oxidation relates best to measures of glucose metabolism. Front. Physiol. *14*, 1172675. https://doi.org/10.3389/fphys.2023.1172675.

50. Portincasa, P., Grattagliano, I., Lauterburg, B.H., Palmieri, V.O., Palasciano, G., and Stellaard, F. (2006). Liver breath tests non-invasively predict higher stages of non-alcoholic steatohepatitis. Clin. Sci. *111*, 135–143. https://doi.org/10.1042/cs20050346.

51. Giacalone, A.G., Merritt, M.E., and Ragavan, M. (2022). Ex Vivo Hepatic Perfusion through the Portal Vein in Mouse. J. Vis. Exp. *181*, e63154.

52. Mahar, R., Zeng, H., Giacalone, A., Ragavan, M., Mareci, T.H., and Merritt, M. (2021). HDO Imaging of the Rat Brain Following Metabolism of [$^2H_7$] glucose. Magn. Reson. Med. *85*, 2049–3059. https://doi.org/10.1002/mrm.28700.

53. Dixon, W.T. (1984). Simple proton spectroscopic imaging. Radiology *153*, 189–194. https://doi.org/10.1148/radiology.153.1.6089263.

54. Peng, X.G., Ju, S., Qin, Y., Fang, F., Cui, X., Liu, G., Ni, Y., and Teng, G.J. (2011). Quantification of liver fat in mice: comparing dual-echo Dixon imaging, chemical shift imaging, and 1H-MR spectroscopy. J. Lipid Res. *52*, 1847–1855. https://doi.org/10.1194/jlr.D016691.

55. Kleiner, D.E., Brunt, E.M., Van Natta, M., Behling, C., Contos, M.J., Cummings, O.W., Ferrell, L.D., Liu, Y.C., Torbenson, M.S., Unalp-Arida, A., et al. (2005). Design and validation of a histological scoring system for nonalcoholic fatty liver disease. Hepatology *41*, 1313–1321.

STAR★METHODS

KEY RESOURCES TABLE

REAGENT or RESOURCE	SOURCE	IDENTIFIER
Antibodies		
CPT1 Primary Antibody	Santa Cruz Biotechnology	Cat#sc-393070; RRID:AB_3075326
COXI-V Primary Antibody	Cell Signaling Technology	Cat#4844; RRID:AB_2085427
GAPDH Primary Antibody	Cell Signaling Technology	Cat#2118; RRID:AB_561053
ACADL/LCAD Primary Antibody	Abcam	Cat#ab128566; RRID:AB_11141244
8-oxo-dG Primary Antibody	R&D Systems	Cat#4354-MC-050; RRID_AB1857195
TFAM Primary Antibody	Invitrogen	Cat#PA5-29571; RRID_AB2547047
4-Hydroxynonenal Primary Antibody	Invitrogen	Cat#MA5-27570; RRID_AB2735095
Goat Anti-Mouse Secondary Antibody (Alexa Fluor Plus 594)	Invitrogen	Cat#A32742; RRID_AB2762825
Goat Anti-Rabbit Secondary Antibody (Alexa Fluor Plus 647)	Invitrogen	Cat#A32733; RRID_AB2633282
Total OXPHOS Rodent WB Antibody Cocktail	Abcam	Cat#ab110413; RRID_AB2629281
Chemicals, peptides, and recombinant proteins		
Lidocaine	Patterson Veterinary	Cat#07-869-7525
Heparin	McKesson Medical Surgical	Cat#949512
$[D_{15}]$octanoate	Sigma Aldrich	Cat#448214
O_2 Gas	Airgas	Cat#OX USP200
95% O_2/5% CO_2 Gas	Airgas	Cat#Z02OX9511900099
D_2O	Cambridge Isotope Laboratories	Cat#DLM-4
Acetonitrile	Fisher Scientific	Cat#A21
Isopropanol	Fisher Scientific	Cat#AC423830040
Methoxyamine HCl in Pyridine (MOX Reagent)	Thermo Scientific	Cat#TS-45950
MTBSTFA	Fisher Scientific	Cat#50-442-893
Hydroxylamine HCl in Pyridine	Fisher Scientific	Cat#AC170361000
Propionic Anhydride	Sigma Aldrich	Cat#240311
Ethyl Acetate	Fisher Scientific	Cat#E145
1x RIPA Lysis Buffer	Thermo Fisher Scientific	Cat#J62725.AP
BSA Protein Standard	Thermo Fisher Scientific	Cat#23209
Bradford Reagent	Bio-Rad Laboratories	Cat#5000006
TRIzol	Invitrogen	Cat#15596026
SYBR Green PCR Master Mix	Applied Biosystems	Cat#4309155
Protease and Phosphatase Inhibitors	Thermo Fisher Scientific	Cat#78440
Bolt 8% Bis-tris Plus Gels	Invitrogen	Cat#NW00087BOX
Nitrocellulose Membrane	Bio-Rad Laboratories	Cat#1620115
Mannitol	Fisher Scientific	Cat#AA3334236
Sucrose	Fisher Scientific	Cat#S5-500
HEPES	Fisher Scientific	Cat#AAA1477718
EDTA	Fisher Scientific	Cat#S311-500
Fatty Acid Free BSA	Sigma Aldrich	Cat#126575
KCl	Fisher Scientific	Cat#AA1159530
K_2HPO_4	Fisher Scientific	Cat#01-337-798
$MgCl_2$	Fisher Scientific	Cat#M33-500
EGTA	Fisher Scientific	Cat#32-462-625GM
ADP	Fisher Scientific	Cat#NC0623142

(*Continued on next page*)

Continued

REAGENT or RESOURCE	SOURCE	IDENTIFIER
NaCl	Fisher Scientific	Cat#S271-500
Standard Rodent Maintenance Diet	Teklad Global	Cat#2918
High Fat Diet	Research Diets	Cat#D12492
Low Fat Diet	Research Diets	Cat#D12450J
4% Paraformaldehyde in PBS	Fisher Scientific	Cat#AAJ61899AK
70% Histological Grade Ethanol	Fisher Scientific	Cat#HC-1000-1GL
IGEPAL CO-630	Sigma Aldrich	Cat#542334
Xylenes	Fisher Scientific	Cat#X3P-1GAL
Histo-Clear	Fisher Scientific	Cat#50-329-47
Citrate	Millipore Sigma	Cat#251275
PBS	Fisher Scientific	Cat#10-010-031
PBST	Fisher Scientific	Cat#50-195-825
ReadyProbes^{TM} 2.5% Normal Goat Serum (1X)	Thermo Fisher Scientific	Cat#R37624
Critical commercial assays		
Miniprep Kit	Bio-Rad Laboratories	Cat#7326100
cDNA Synthesis Kit	Bio-Rad Laboratories	Cat#1708890
Pierce BCA Protein Assay Kit	Thermo Fisher Scientific	Cat#23227
Triglyceride Reagent	Millipore Sigma	Cat#T2449
ALT (SGPT) Liquid Reagents	Pointe Scientific	Cat#A7526625
AST (SGOT) Liquid Reagents	Pointe Scientific	Cat#A7561150
Experimental models: Organisms/strains		
Mouse: C57BL/6J	The Jackson Laboratory	Cat#000664; RRID:IMSR_JAX:000664
Rat: Sprague Dawley	Charles River Laboratory	Cat#001
Oligonucleotides		
Hmgcs2	Integrated DNA Technologies	Forward: GAC TTC CTG TCA TCC AGC Reverse: GGT GTA GGT TTC TTC CAG C
Lcad	Integrated DNA Technologies	Forward:TCAATGGAAGCAAGGTGTTCA Reverse:GCCACGACGATCACGAGAT
Software and algorithms		
ImageJ	NIH	v1.53k
XCalibur	Thermo Fisher Scientific	v4.1
INCA	Vanderbilt University	v1.9
MATLAB	Mathworks	v9.11.0.1809720
Rstudio	Posit, PBC	v1.3.1073
Bruker Topspin	Bruker	v3.6.2
Paravision6	Bruker	v6.0.1
Mestrenova	Mestrelab Research	v14.0.1–23284
Python	The Python Software Foundation	v3.8
Python Library: numpy	The Python Software Foundation	v1.19.2
Python Library: pandas	The Python Software Foundation	v1.1.3
Python Library: matplotlib	The Python Software Foundation	v3.3.2
Python Library: nmrglue	The Python Software Foundation	v0.8
Inkscape	Inkscape	v0.92.2

EXPERIMENTAL MODEL AND STUDY PARTICIPANT DETAILS

Animals

Experiments involving mice (in bred strains used were C57BL/6J (Stock No. 000664, RRID:IMSR_JAX:000664)) were handled in compliance with University of Florida Institutional Animal Care and Use Committee (protocol number #201909320). All male mice were 8–10 weeks old at the start of diets. Prior to arrival in the animal housing facility, animals were tested and determined to be pathogen and opportunist free by the Jackson Laboratory. No prior experiments were performed on these animals. Animals were maintained in HEPA filter ventilated housing from arrival to the end of the study.

METHOD DETAILS

Liver perfusion

Mice were maintained on either an LFD (10% Kcal from fat, D12450J, Research Diets, New Brunswick New Jersey) or HFD (60% Kcal from fat, D12492, Research Diets New Brunswick New Jersey) for 16 weeks and were weighed every week. At 16 weeks on the diet, mice were overnight fasted 12–14 h before being anesthetized using isoflurane followed by an intraperitoneal injection of 200 μL of saline with 200 units of heparin. Approximately 10 min after heparin injection, a celiotomy was performed under anesthesia. Lidocaine was administered subcutaneously prior to making the first incision that exposed the liver and the portal vein. The portal vein was then cannulated, and perfusion was started. The liver was then excised from the body and connected to the glass perfusion column,[51] which was moved into the bore of a 600 MHz NMR magnet.

Livers were perfused with Krebs – Henseleit buffer (25 mM $NaHCO_3$, 112 mM NaCl, 4.7 mM KCl, 1.2 mM $MgSO_4$, 1.2 mM KH_2PO_4, 1.25 mM $CaCl_2$, and 0.5 mM sodium-EDTA), 1 mM sodium lactate, and 0.1 mM sodium pyruvate during magnet shimming. The system was switched to recirculating mode after magnetic field shimming (~12–16 min), and the perfusate solution was supplemented with 1.2 mM sodium-[D_{15}]octanoate. Perfusate was oxygenated using 95% O_2/5% CO_2 mixed gas (Airgas) for the duration of perfusion. Oxygen consumed by the liver during perfusion was measured every 10 min using an Oxygraph+ setup (Hansatech Instruments, UK). At the end of perfusion, the livers were freeze clamped using liquid nitrogen and stored at -80°C. One mL perfusate samples were collected every 10 min after switching to the [D_{15}]octanoate perfusate for analysis of HDO production and GC-MS metabolomics. The number of mice used in each group were LFD mice (n = 5) and HFD mice (n = 5).

NMR spectroscopy

Deuterium spectra were collected in a custom built 20 mm broadband probe (QOneTec, Switzerland) installed in a 14 T (92 MHz ^{2}H frequency) magnet equipped with an Avance III NMR console (Bruker Biospin, USA). Deuterium spectral acquisition began 1 min prior to switching to perfusate with the [D_{15}]octanoate. Magnetic field shimming was executed by manual adjustment while observing the linewidth of the ^{23}Na signal associated with the perfusate. Typically, linewidths of around 18 Hz in ^{23}Na spectrum were achieved with ^{2}H spectral linewidths also averaging ~18 Hz. ^{2}H spectra (spectral width of 25.0192 ppm; 4096 data points) were recorded using a 90° pulse centered on the HDO resonance (nominally, 4.7 ppm) with ^{1}H decoupling (WALTZ65; B1 = 4.5 kHz) during the acquisition (acquisition time = 0.887 s) and a repetition time of 4.9 s with 16 scans per 1.33 min time point and up to 128 time points. Spectra were processed with 1.5 Hz exponential line broadening and baseline corrected using a polynomial function. Peak areas of HDO and octanoate were obtained by integration of the 5.4 to 3.8 ppm and 2.4 to -0.3 ppm regions, respectively, with a custom python script.

Gas chromatography – Mass spectrometry

Freeze-clamped samples of the perfused liver were stored at -80°C prior to analysis. Perfused liver samples (110 ± 10 mg) were transferred into 2 mL microcentrifuge tubes with screw caps, and 1.0 mm zirconium oxide homogenization beads were added along with 1 mL of cold degassed acetonitrile:isopropanol:water (3:3:2 v/v/v) solvent mixture. Samples were homogenized with a bead homogenizer (Fastprep-24, M.P. Biomedicals, Irvine, CA) for 3 × 20 s cycles and were cooled on ice for 5 min between each cycle. The samples were then centrifuged at 10,000 x g at 4°C for 30 min. Supernatant (900 μL) was recovered and lyophilized (Thermo Scientific Waltham, MA). The dried precipitate was reconstituted in 150 μL of acetonitrile:water (1:1 v/v) mixture followed by incubation at -20°C for at least 2 h. Reagents, unless otherwise specified, were purchased from Fisher scientific, New Jersey.

MTBSTFA derivatization

For analysis of amino acids, ketones, and TCA cycle intermediates, ~8 mg of liver extract or 20 μL of perfusate were dried down by gentle airstream. The sample was reconstituted in 50 μL of methoxyamine HCL in pyridine (Thermo Scientific, Pennsylvania) for 1.5 h at 30°C with stirring. N-*tert*-Butyldimethylsilyl-N-methyltrifluoroacetamide (MTBSTFA; ProteoSpec MTBSTFA w/1% TBDCMS, Ricca Chemical Company, Texas) (50 μL) was added and samples were incubated at 70°C for 30 min while stirring. After derivatization, 80 μL of the sample was transferred to a GC vial for analysis by GC-MS.

Aldonitrile pentapropionate derivatization

For measurement of sugars eluted during perfusion, 500 μL of perfusate was dried in 0.5 mL V-vials and reconstituted in 50 μL of 20 mg/mL hydroxylamine hydrochloride (CAS# 5470-11-1; Acros organics, New Jersey) in pyridine (CAS#25104, Thermo scientific, Rockford, IL) and stirred at 90° C for 1.5 h. Propionic anhydride (CAS# 240311-50G; Sigma Aldrich, St. Louis, MO) (100 μL) was then added and samples were stirred at 70°C for 30 min. Samples were dried by gentle airstream and then reconstituted in 100 μL of ethyl acetate for GC-MS analysis.

Protein estimation in liver tissue

Protein was extracted from 10 mg of powdered excised mouse liver sample by homogenization with 300 μL of 1X RIPA lysis buffer in a bead homogenizer (Fastprep-24, M.P. Biomedicals, Irvine, CA). Samples were mixed by inversion at 4°C for 2 h. After mixing, the samples were centrifuged at 10,000 x g at 4°C for 30 min before collecting 150 μL of the supernatant. Samples were diluted 15-fold before using 10 μL of diluted liver protein extract with 200 μL of Bradford reagent and incubating for 5 min before quantifying protein absorbance at 595 nm on a 96-well plate against a standard curve of BSA protein standards that ranged from 1.2 to 0.0625 mg/mL.

Expression profiles in liver tissue

For quantitative reverse transcriptase-polymerase chain reaction (QPCR) analysis, frozen liver tissue (~10–15 mg) was homogenized in 600 μL TRIZOL reagent (Invitrogen, Carlsbad, CA) to isolate mRNA using a miniprep kit (Bio-Rad Laboratories Inc., Hercules, CA). A cDNA synthesis kit (Bio-Rad, Hercules, CA) was used to prepare cDNA from 1 μg of mRNA. QPCR was performed utilizing 25 ng of cDNA, 150 nM forward and reverse primers, and 5 μL of SYBR green PCR master mix (Invitrogen, Carlsbad, CA) with *cyclophilin* as the housekeeping gene. Each sample was run in triplicates on a Bio-Rad CFX Real-Time system (C1000 Touch Thermal Cycler).

For Western blot analysis, frozen liver tissue (~10–15 mg) was lysed in 1x RIPA lysis buffer with protease and phosphatase inhibitors. The solution was centrifuged at 15,000 RPM (20,627 G) for 15 min at 4°C. Total protein was analyzed by Pierce BCA protein assay kit (Thermo Fischer Scientific. Waltham, MA). Protein separation by gel electrophoresis was performed using Bolt 8% Bis-tris Plus gels (Invitrogen, Carlsbad, CA) before transfer to a nitrocellulose membrane. The membrane was incubated with the primary antibody overnight followed by incubation with the secondary antibody. Primary antibodies against CPT1A, COXI-V, GAPDH (Cell Signaling Technology, Danvers MA), and LCAD (Abcam, Cambridge, UK) were utilized for this study. Western blot quantification was performed with ImageJ of the respective blots signal relative to GAPDH signal.

Mitochondrial isolation to determine HDO retention

Whole liver was excised from a 12-week-old Sprague-Dawley rat after sacrifice and cut into 1 g pieces before crushing in a Dounce homogenizer in 15 mL of isolation buffer I (225 mM mannitol, 75 mM sucrose, 10 mM HEPES potassium, 1 mM EDTA, 0.1% fatty acid free BSA, pH 7.4) [45] and then centrifuging the homogenate at 1300 x g for 30 min at 4°C. The supernatant was then collected in a new tube and centrifuged at 10,000 x g for 30 min at 4°C. The supernatant was then discarded. The pellet was resuspended in 2 mL of isolation buffer II (225 mM mannitol, 75 mM sucrose, 10 mM HEPES potassium, 0.1 mM EDTA, pH 7.4), transferred to a clean 2 mL centrifuge tube, and centrifuged at 10,000 x g for 30 min at 4°C. The supernatant was then discarded and the pellet was resuspended in 200 μL isolation buffer II. 67 μL of mitochondrial pellet was incubated with 2 mL of incubation buffer (125 mM KCL, 2 mM K_2HPO_4, 5 mM $MgCl_2$, 10 mM HEPES, 10 μM EGTA, pH 7.2) 4mM sodium octanoate ($n = 6$) or 4 mM sodium-[D_{15}]octanoate ($n = 5$) and 0.2 mM of ADP for 5 min at 37°C before taking the buffer and mitochondria and pelleting them out at 10,000 x g for 30 min at 4°C. The supernatant was collected for further analysis of HDO enrichment by NMR and the pellet was subjected to 2 more washes of 1 mL of isolation buffer I and two more centrifugations at 10,000 x g fro 30 min at 4°C before resuspending the pellet in 300 μL of acetonitrile with a 2.5 mM [D_4]pyrazine standard to lyse the pellet and free internal water storage for HDO analysis.

Deuterium magnetic resonance imaging

Initial metabolic images were acquired as in Mahar et al. 2021 [52] with the following modifications: a 26 mm deuterium saddle coil was used instead of 14 mm deuterium surface coil, the coil was placed under the animal's abdomen, and the average time for image collection was 26 min instead of 13 min. Three 12 week old male C57BL/*6J* mice were placed in the magnet and a background image was taken. After injection with 0.675 mg/g [D_{15}]octanoate in a 180 μL volume through a catheterized tail vein, the imaging protocol continued (Figure S5). Two point Dixon (2PD) imaging was performed with respect to HDO and [D_{15}]octanoate.[53,54]

For the MRI diet study, 8-week-old C57BL/6J mice were maintained on a standard rodent maintenance diet (Teklad global protein 18%, with 18% of calories from fat) or an HFD (60% Kcal from fat, Research diets) for up to 36 weeks (60 HFD and 40 chow at start of diet). Food consumption and animal weight were measured weekly for both mice cohorts. Imaging sessions took place at 0, 8, 17, 24 and 36 weeks of diet with a goal of 5 animals for 16–18 h fasted or *ad libitum* fed on either diet. For each imaging session, mice were anesthetized with isoflurane, then weighed and the tail vein was catheterized. Subsequently, the animal was placed in a 26 mm linear deuterium saddle coil while under isoflurane anesthesia and the coil was tuned to −42 to −55 db using a network analyzer. Then the animal was placed within the 11 T, horizontal bore magnet. After centering the mouse's liver within the coil and shimming down to an HDO peak linewidth of 80 Hz or less, background single pulse, selective pulse fast low angle shot gradient (SPFLASH) of HDO and [D_{15}]octanoate internal standards, liver SPFLASH spectra and ^{2}H FLASH images were acquired (Figure S6). Slice thickness was adjusted to span the liver region within an axial slice without overlap with the heart or kidneys (between 8 and 14 mm). Afterward the mice were injected with 0.33 mg/g [D_{15}]octanoate, with a maximal injection of <14 mg. *Ad libitum* fed animals were injected at 10:00a.m. ± 30 min and ~18 h-fasted mice were injected at 2:00p.m. ± 30 min. Injections were performed at a rate of 40–50 μL per minute with a 0.25 M sodium-[D_{15}]octanoate solution pH 7.2. During and after injection, several single pulse, unlocalized spectra and SPFLASHs of the phantom and tissue were obtained to view import and utilization kinetics. The 2PD imaging was acquired for HDO versus [D_{15}]octanoate signal from 17 to 44 min. The 2PD image was followed by a whole torso slice selective excitation of the HDO phantom first then the [D_{15}]octanoate phantom second, and SPFLASH of the liver region last (occurring between 45- and 52 min post-injection). This was followed by a full spectral image at 62 to 90 min and then a repeat of the spectroscopy that followed the 2PD imaging. Finally, a follow up ^{1}H axial image was obtained for co-registration.

Localization of HDO to the mitochondrial compartment

The results from the perfused liver indicated that HDO was a quantitative readout of β-oxidation. However, generalization of the method to *in vivo* requires that HDO is generated and retained in the liver, because octanoate is oxidized in many tissues in the whole animal. On the basis of the accumulation of deuterated signal in the livers of mice injected into the tail vein with [D_{15}]octanoate (Figure 4), we hypothesized that HDO does not freely diffuse through the mitochondrial membrane. To provide sufficient material for analysis, we isolated mitochondria from livers of Sprague-Dawley rats and assessed β-oxidation of either deuterated or unlabeled octanoate. Hepatic isolated mitochondria were incubated with 4 mM [D_{15}]octanoate and subjected to two, 1-mL washes with natural abundance H_2O buffer over the course of 1.5 h at room temperature to wash out freely diffusing deuterated water. We determined the amounts of HDO released into the buffer and associated with the mitochondrial pellet (Figure S10). Compared to the HDO concentration in the buffer from mitochondria incubated with unlabeled octanoate, the buffer from the mitochondria incubated with [D_{15}] octanoate exhibited an insignificant increase. In contrast, we detected a ~50% increase in HDO in the mitochondrial pellet following incubation in [D_{15}]octanoate, thus, confirming that HDO produced by metabolism of octanoate accumulated in mitochondria of rodent livers.

Because mitochondria are the site of β-oxidation and the mitochondrial membranes tightly control H^+ flux to enable chemiosmotic ATP production, we hypothesized that mitochondria were the source of the HDO signal that did not rapidly diffuse. Assuming free diffusion of the water, the dilution factor after 2 subsequent washes of 1 mL exceeds 1000-fold. A 1000-fold dilution should return mitochondrial HDO enrichment to natural abundance, as the greatest enrichment observed *in vivo* was only 3-fold natural abundance of HDO (Figure S7). The incubation buffer measured a nonsignificant ~6% increase in HDO signal from [D_{15}]octanoate treated mitochondria compared to unlabeled sodium octanoate (Figure S10A), which indicated negligible export of HDO. However, after two washes a ~50% increase in HDO signal for the [D_{15}]octanoate-exposed mitochondrial pellet compared to the unlabeled octanoate-exposed mitochondrial pellet was maintained (Figure S10B). If the mitochondria could freely exchange HDO, the added [D_{15}]octanoate would have to produce a 20% enrichment in HDO in the mitochondria to produce the observed enrichment after a ~1000-fold dilution. We note that malate, a hydride receptor in the TCA cycle that exists in rapid equilibrium with oxaloacetate, was only ~0–4% enriched in ^{2}H (Figure S3). If the mitochondrial compartment had a 20% enrichment, malate should reflect this fact. Collectively, these observations showed that diffusion of HDO across the mitochondrial membrane is limited on this time scale.

Histological assessment of steatosis in diet mice

The medial lobe of the liver located to the right of the gall bladder was collected for histological assessment of liver disease and steatosis. The excised tissue was incubated in a 2% formalin solution overnight at room temperature before transfer to fresh 70% histological grade ethanol the following day and another overnight incubation at room temperature. On day two after collection the medial lobe was transferred to a fresh solution of 70% histological grade ethanol and incubated overnight at room temperature. On day three post collection the tissue, in 70% histological grade ethanol, was placed within a 4°C fridge until it was submitted to the University of Florida Molecular Pathology Core to be paraffin embedded, cut onto a slide and stained via a hematoxylin and eosin (H&E) stain protocol or left unstained for subsequent protocols. The stained tissue was imaged within the University of Florida Molecular Pathology Core and images were processed using ImageJ to calculate the percentage steatosis by lipid fraction area. Five subregions of each liver slice were utilized to determine the percent steatosis score. Lipid fraction area was determined by calculating the white space in the liver fraction with a grayscale cutoff of 190–255 and manual removal of white space due to arterial and venous fractions of the tissue. Whole slides were analyzed by a trained pathologist and assigned a MASLD activity score (MAS) based on the presence or absence of steatosis, hepatocyte cell ballooning and lobular inflammation.[55]

Liver triglyceride assay

100 mg of freeze clamped powdered liver tissue was homogenized in 1 mL of IGEPAL CO-630 – average M_n −617 (Sigma Aldrich, St. Louis, MO). Samples were heated at 80°C in a metal bead bath for 5 min then cooled to room temperature and this process was repeated twice until the solution was cloudy. The solution was centrifuged for 2 min at 10,000 x g at room temperature to remove insoluble material. 100 μL of supernatant was collected and diluted 100-fold with water before assay. 1.5 μL of the diluted sample was added into a wells in a 96 well plate. Samples were raised to a final volume of 50 μL with Triglyceride Assay Buffer (CAS# MAK266, Sigma Aldrich, St. Louis, MO). 2 μL of Lipase was added to each sample and was incubated for 20 min at room temperature to convert triglyceride to glycerol and fatty acids with the plate shaken manually every 10 min. Then 50 μL of master reaction mix was added to each well and the plate was incubated in the dark with occasional stirring every 10 min for 30 min. Subsequently, absorbance at 570 nm was measured by a plate reader. The absorbance was blank corrected against assay buffer and quantified relative to a standard curve of 0.1, 0.4, 1.6, 6.4 and 10 nmol's per well.

Immunofluorescence

Standard immunofluorescence procedures were performed on 10 μm liver slices from formalin-fixed, paraffin-embedded blocks. Three independent experiments were performed. Briefly, slides were placed at 60°C for 1 h and dewaxing was performed with xylenes or Histo-Clear. Heat-induced epitope retrieval consisted of placing the slides in a 95°C water bath for 30 min in a citrate buffer. After cooling for 30 min, slides were permeabilized with rinses of 5 min in PBS, 30 min in PBST, and 5 min in PBS. Slides were blocked with ReadyProbes 2.5% Normal Goat Serum (1X) (ThermoFisher Scientific, R37624). Primary antibodies used were: 8-oxo-dG to bind to 8-hydroxy-2′- deoxyguanosine (n = 13,12,18,22 sections for 8 weeks chow or HFD and 24 weeks chow or HFD respectively) (R&D Systems, cat # 4354-MC-050, 1:200), TFAM (n = 13,12,18,20 sections for 8 weeks chow or HFD and 24 weeks chow or HFD respectively) (Invitrogen, cat # PA5-29571, 1:200), and 4-Hydroxynonenal (n = 9,11,16,16 at 8 weeks for chow or HFD and 24 weeks for chow or HFD) (Invitrogen, cat # MA5-27570, 1:50). Goat Anti-Mouse (Invitrogen, A32742 (Alexa Fluor Plus 594), 1:2000) and Goat Anti-Rabbit (Invitrogen, A32733 (Alexa Fluor Plus 647), 1:2000) secondary antibodies were used. Slides were imaged on a Revolve microscope at 20× magnification. Quantification used the total fluorescent signal in each channel normalized to DAPI nuclear signal and was performed in ImageJ. Statistical significance was assessed with individual t-tests ($p < 0.05$) in GraphPad Prism.

ALT and AST

ALT and AST abundance in the blood was assayed according to the instructions for Pointe Scientific ALT (SGPT) Liquid Reagents (n = 10,9,7,6,8,10 for baseline, 8.5 weeks on HFD, 17 weeks on chow or HFD and 24 weeks on chow or HFD) (Pointe Scientific, cat # A7526625) and AST (SGOT) Liquid Reagents (n = 10,9,6,8,10,6 for baseline, 8.5 weeks on HFD, 17 weeks on chow or HFD and 24 weeks on chow or HFD) (Pointe Scientific, cat # A7561150).

QUANTIFICATION AND STATISTICAL ANALYSIS

Metabolite analysis by GC-MS

After the derivatization reaction (aldonitrile pentapropionate or MTBSTFA) was completed, 5 μL of each sample was pooled together to make a “pooled sample” for a given derivatization batch and 80 μL of each individual sample were loaded into a 150 μL glass insert (CAS#13-622-207, Thermo scientific, Florence, KY) inside of a GC vial with a 9 mm PTFE/red rubber septum (CAS#C4000-30, Thermo scientific, Rockwood, TN). Samples were placed in an AI/AS 1300 autosampler prior to auto injection. A 1 μL injection volume was used for each sample into the injection port of the Trace1310 Ga chromatography system (Thermo Scientific, PA). The injection was performed in splitless mode with a splitless single taper liner, splitless time of 60 s, and injection port temperature of 250° C. Column flow was set at 1 mL/min through a 30 m RTX-5MS integra Guard column (Crossbond 5% diphenyl/95% dimethyl polysiloxane CAT# 12623-127, Restek PA) and 10 m guard column. For MTBSTFA-derivatized samples, the following parameters were used: 60°C hold time = 1 min, ramp of 15°C/min up to 320°C followed by a 5-min bakeout/cleaning phase at 320°C. Aldonitrile pentapropionate–derivatized samples were run on the same GC-MS instrument with the following parameters: start temperature of 80°C with a hold time = 1 min, 20°C per minute ramp up to 280°C, followed by a 5-min bakeout at 280°C. For all samples, the transfer line was maintained at 280°C and the ion source was maintained at 230°C. The solvent delay on the mass spectrometer was set to 10 min for MTBSTFA-derivatized samples and 8 min for aldonitrile pentapropionate–derivatized samples. An m/z filter of 40–600 mass-to-charge ratio was used for spectral acquisition. Individual metabolites were identified and quantified by area using their known quantification ions (Table S8). Concentrations were assessed against an eight-point standard curve that ranged from 50 to 1600 ng of the metabolite of interest.

Peak integration

Peak areas were integrated using Xcalibur (version 4.1) batch processing with genesis peak fitting, a 5-s time interval, height cutoff at 5.5% of the peak with valley detection enabled, and a signal to noise (S/N) cutoff threshold of 3.

Isotopic ratio and fractional enrichment

The isotopic ratio of each metabolite for its given quantitation ion was calculated as the ratio of intensity of each mass isotopomer (m_i) to the sum of all mass isotopomers. The isotopic ratio distribution was then corrected for natural abundance as previously described using the Isotopomer Network Compartmental Analysis (INCA) software [30,50].

INCA metabolic modeling

A metabolic model (Table S1) was designed in INCA to track production of HDO through β-oxidation and TCA cycle turnover. To provide a boundary condition dependent on total, quantitative, oxidative flux, the model was supplied with measurements of oxygen consumption, fractional enrichment and pool sizes for selected TCA cycle intermediates and the ketone 3-hydroxybutyrate, rates of gluconeogenesis and ketogenesis based on the final concentration in the effluent, and the fold change increase in the HDO peak over the course of the experiment.

The label in citrate derives from deuterated acetyl-CoA generated during β-oxidation in this system (Figure 3B; Table S1). Ketones are derived from two individual acetyl-CoA units and thus can be labeled if either one of the acetyl-CoA units is labeled. Consequently, the probability of attaining a labeled ketone is nearly double that of the acetyl-CoA fractional enrichment. Thus, it could be estimated that the acetyl-CoA fractional enrichment is 33.5%. However, M+1 generated acetyl-CoA units (Figure S1) have a 1/3 chance of isotopic loss if they act as a nucleophile in the generation of the ketone 3-hydroxybutyrate. If we assume that M+1 generated acetyl CoA units have an equal chance of being an electrophile or a nucleophile in the generation of ketones, then we would expect a loss in ketone enrichment equivalent to 1/6th of the M+1 fractional enrichment (~4%). Thus, an additional 2% can be added to the overall acetyl-CoA enrichment to yield a 35.5% enrichment. Citrate enrichment is similarly affected by M+1 deuterated acetyl-CoA label loss during nucleophilic attack by a 1/3 ratio. In this situation the M+1 fractional enrichment (23.4%) of citrate is estimated to be 66% of the actual M+1% fractional enrichment. To get an accurate estimate of M+1 acetyl-CoA fractional enrichment, lost citrate M+1 enrichment must be added back in by taking 50% of the current citrate M+1 fractional enrichment. After adjustment for label loss the total enrichment from acetyl-CoA in citrate is estimated to be 38.8%. After correction, the fractional enrichment of acetyl-CoA is ~35–39% (Figures 3C and 3D; Table S1). Label in the TCA cycle decreased from citrate (25%) to fumarate (0–2%) with glutamate and succinate at 18% and 8%, respectively (Figure 3C) (Figure S3). Based on these fractional enrichments the deuterium label is liberated before the beginning of the second turn of the TCA cycle. Therefore, all label in the TCA cycle represents first pass kinetics.

Deuterium magnetic resonance imaging

Deuterium images were overlaid with ^{1}H images and the ratio of deuterium signal over the liver region relative to the HDO phantom was used to determine the fold change in average signal before and after [D_{15}]octanoate injection as in (Equation 1a). The fold change was then corrected for total signal change by multiplying the fold change by the area of the liver and the depth of the image (total volume) (Equation 1b). Normalization to the slice thickness is necessary, as the mouse liver ranged between 6 and 14 mm in depth in the ^{1}H images. The total fold change was converted into the total signal fold change per mg dose of [D_{15}]octanoate injected to accurately assess total β-oxidation per mg dose and total β-oxidative capacity of the liver (e.g., how much HDO can a liver liberate per mg deuterated fatty acid) (Equation 1c). An estimate of the β-oxidative efficiency of the liver was calculated by dividing the total β-oxidative capacity by the liver mass (Equation 1d).

$$HDO\ fold\ change = \frac{2PD\ mean\ liver\ HDO\ signal}{2PD\ mean\ HDO\ phantom\ signal} \Bigg/ \frac{2H\ FLASH\ mean\ liver\ signal\ pre-injection}{2H\ FLASH\ mean\ HDO\ phantom\ signal} \qquad \text{(Equation 1a)}$$

$$Total\ HDO\ signal\ increase = HDO\ fold\ change * liver\ area * image\ depth \qquad \text{(Equation 1b)}$$

$$Total\ \beta - oxidative\ capacity = \frac{Total\ HDO\ signal\ increase}{mg\ [\mathrm{D}_{15}]\mathrm{octanoate}} \qquad \text{(Equation 1c)}$$

$$\beta - oxidative\ efficiency = \frac{Total\ \beta - oxidative\ capacity}{g\ liver} \qquad \text{(Equation 1d)}$$

Statistical analysis

For comparison of dietary timepoints and binary groups students t.tests (two-tailed) were used to establish significance with an $\alpha = 0.05$. As the number of variables was limited, no correction for multiple variables was used. For HDO production and kinetic measurements significance was determined based on analysis of covariance (ANCOVA) via in lab scripts using Rstudio and the in-built "aov" function.

Software

All NMR data processing was carried out using Bruker Topspin (3.6.2+) or Mestrenova (v14.0.1–23284 (Mestrelab Research S.L., Santiago, Spain). Image processing for DMRI was carried out using in lab designed MATLAB (Mathworks, Natick, MA) scripts and ImageJ. Figures were prepared using in house python (v3.8) scripts: Libraries utilized were numpy (v1.19.2), pandas (v1.1.3), matplotlib (v3.3.2), and nmrglue (v0.8), and Inkscape (v0.92.2). Metabolic modeling was performed using INCA v1.9.[28]